Molecular Psychiatry (2021) 26:5441–5463
https://doi.org/10.1038/s41380-020-0787-4

ARTICLE

Shedding a new light on Huntington's disease: how blood can both propagate and ameliorate disease pathology

Marie Rieux[1,2] · Melanie Alpaugh[1,3] · Giacomo Sciacca[1,3] · Martine Saint-Pierre[1] · Maria Masnata[1,3] · Hélèna L. Denis[1,3] · Sébastien A. Lévesque[1,2] · Frank Herrmann[4] · Chantal Bazenet[4] · Alexandre P. Garneau[5,6] · Paul Isenring[5] · Ray Truant[7] · Abid Oueslati[1,2] · Peter V. Gould[8] · Anne Ast[9,10] · Erich E. Wanker[9,10] · Steve Lacroix[1,2] · Francesca Cicchetti[1,3]

Received: 7 January 2020 / Revised: 6 May 2020 / Accepted: 13 May 2020 / Published online: 8 June 2020

Abstract

Huntington's disease (HD) is a monogenic neurodegenerative disorder resulting from a mutation in the *huntingtin* gene. This leads to the expression of the mutant huntingtin protein (mHTT) which provokes pathological changes in both the central nervous system (CNS) and periphery. Accumulating evidence suggests that mHTT can spread between cells of the CNS but here, we explored the possibility that mHTT could also propagate and cause pathology via the bloodstream. For this, we used a parabiosis approach to join the circulatory systems of wild-type (WT) and zQ175 mice. After surgery, we observed mHTT in the plasma and circulating blood cells of WT mice and post-mortem analyses revealed the presence of mHTT aggregates in several organs including the liver, kidney, muscle and brain. The presence of mHTT in the brain was accompanied by vascular abnormalities, such as a reduction of Collagen IV signal intensity and altered vessel diameter in the striatum, and changes in expression of Glutamic acid decarboxylase 65/67 (GAD65-67) in the cortex. Conversely, we measured reduced pathology in zQ175 mice by decreased mitochondrial impairments in peripheral organs, restored vessel diameter in the cortex and improved expression of Dopamine- and cAMP-regulated phosphoprotein 32 (DARPP32) in striatal neurons. Collectively, these results demonstrate that circulating mHTT can disseminate disease, but importantly, that healthy blood can dilute pathology. These findings have significant implications for the development of therapies in HD.

Introduction

Huntington's disease (HD) is a monogenic neurodegenerative condition which presents with a complex symptomatology of motor, cognitive and psychiatric impairments [1, 2] that progresses to death 10 to 30 years after clinical onset [3]. The main neuropathological

These authors contributed equally: Marie Rieux, Melanie Alpaugh

Supplementary information The online version of this article (https://doi.org/10.1038/s41380-020-0787-4) contains supplementary material, which is available to authorized users.

✉ Francesca Cicchetti
francesca.cicchetti@crchudequebec.ulaval.ca

[1] Centre de Recherche du CHU de Québec—Université Laval, Axe Neurosciences, 2705 boulevard Laurier, Québec, QC G1V 4G2, Canada

[2] Département de Médecine Moléculaire, Université Laval, 1050 avenue de la Médecine, Québec, QC G1V 0A6, Canada

[3] Département de Psychiatrie & Neurosciences, Université Laval, 1050 avenue de la Médecine, Québec, QC G1V 0A6, Canada

[4] Evotec SE, Essener Bogen 7, 22419 Hamburg, Germany

[5] L'Hôtel-Dieu de Québec—Université Laval, Axe Endocrinologie et Néphrologie, 10 rue McMahon, Québec, QC G1R 2J6, Canada

[6] Ecole de Kinésiologie et des Sciences de l'Activité Physique, Université de Montréal, 2100 boulevard Édouard-Montpetit, Montréal, QC H3T 1J4, Canada

[7] Department of Biochemistry and Biomedical Research, McMaster University, 1280 Main Street West, Hamilton, ON L8S 4L8, Canada

[8] Département d'Anatomopathologie et de Cytologie, Centre Hospitalier Affilié Universitaire de Québec, Hôpital de l'Enfant-Jésus, 1401 18ème rue, Québec, QC G1J 1Z4, Canada

[9] Neuroproteomics, Max Delbrueck Center for Molecular Medicine, 13125 Berlin, Germany

[10] Berlin Institute of Health, 10178 Berlin, Germany

hallmarks of HD relate to extensive cell loss in the striatum as well as a host of brain structures, in particular the cerebral cortex [4, 5]. Disease is driven by an autosomal dominant pattern of inheritance and is caused by a pathological CAG repeat expansion exceeding 35 in exon 1 of the *huntingtin* gene (*HTT*), which encodes for huntingtin (HTT), a ubiquitously expressed cytoplasmic protein [6]. This CAG elongation leads to the production of the mutant huntingtin protein (mHTT), which is characterized by an extended polyglutamine (polyQ) stretch [7, 8]. While mHTT is classically considered to drive pathology from within cellular populations, it is also found in the cerebrospinal fluid (CSF), plasma and extracellular matrix [9–13]. There is evidence that both peripheral and extracellular mHTT may contribute to, as well as *amplify*, the disease phenotype.

Although the central nervous system (CNS) is especially vulnerable to mHTT-induced toxicity [14], several peripheral abnormalities have been described in HD, including changes in protein metabolism in skeletal muscles [15], reduction in hepatic mitochondrial function [16] and loss of lower limb strength [17]. Notably, accumulating evidence suggests that early changes within the peripheral immune system may critically contribute to CNS-associated pathology. For example, the presence of mHTT in peripheral monocytes has been reported to correlate with disease stage and progression of caudate atrophy in patients [18]. In fact, alterations in components of the immune system (e.g., peripheral cytokine levels) have been detected as early as 16 years prior to the predicted onset of clinical symptoms [19]. Bone marrow transplantation has also been shown to confer some improvement on behavioral deficits in mouse models of HD (YAC128 and BACHD) [20], implying that deletion of peripheral cells containing mHTT can improve central pathology.

The toxicity of mHTT has long been established but in recent years, a possible new mechanism has begun to emerge; the concept that mHTT can propagate between cells and template pathology in a prion-like fashion [21, 22]. This theory builds, in part, on our observations that mHTT aggregates can be found within fetal striatal transplants in HD patients years after they were grafted [11]. More recently, we have shown that fibroblasts or induced pluripotent stem cells (iPSCs) derived from HD patients injected into the ventricular system result in both motor and cognitive impairments in wild-type (WT) mice. We have additionally shown that WT mice injected with fibrillar forms of mHTT exon 1 protein fragments with a 48-glutamine repeat (Httex1-Q48) into the cortical parenchyma developed cognitive deficits, while similar injections into the lateral ventricles of newborn R6/2 transgenic HD mice precipitated motor and cognitive phenotypes [23]. Another salient finding from this work was the presence of fibrillar mHTT in structures remote from the injection site, suggesting the spreading of mHTT [11, 13]. In an HD drosophila model, it was explicitly demonstrated, using a FRET-based aggregate seeding assay, that the smaller Httex1-Q97 aggregates are seeding competent [24]. The clinical relevance of these findings is highlighted by the detection of such forms in the most affected cerebral structures (i.e., striatum and cortex) of HD patient brains.

The seeding capacity of mHTT has now been shown along with neuronal toxicity in several cell models [22, 25] as well as in in vivo paradigms (i.e. mouse, drosophila and *C. elegans*) [9, 24, 26–28] and a number of putative mechanisms of spread have been postulated, including trans-synaptic and paracrine transmission, as well as exocytosis. Although compelling evidence has been provided for some of these mechanisms in HD, none of these studies have evaluated transmission from sources outside of the CNS. Here, we sought to investigate the role of circulating mHTT and the potential contribution of peripheral pathways to disease pathology using a parabiosis approach where we joined the circulatory systems of a well-established mouse model of HD, the zQ175 mouse, with WT littermates. Our study reveals that blood not only serves as a vehicle of propagation for mHTT, but also that healthy blood can rescue some of the pathology seen in HD mice.

Materials and methods

Animals

zQ175 mice (B6J.129S1-Htttm1Mfc/190ChdiJ) and WT littermate control mice were purchased from The Jackson Laboratory (Bar Harbor, ME, USA) and maintained in an in-house colony at the Centre de Recherche du CHU de Québec – Université Laval (CRCHUQ-UL, Québec, QC, Canada). zQ175 mice express a chimeric mouse/human exon 1 *mHTT* with approximately 190 CAG repeats and display an HD-like phenotype [29]. Female mice were used for all studies as male mice, including littermates, are more prone to aggressive behavior which is incompatible with the long-term pairing required by the parabiosis procedure [30]. β-actin Green Fluorescent Protein (GFP) mice were provided by Dr. Serge Rivest at the CRCHUQ-UL. All mice were maintained in a temperature-controlled room (~23 °C) with a 12/12 h (h) light/dark cycle and *ad libitum* access to food and water. Animal handling, surgeries and all other procedures were completed in accordance with the guidelines of the Canadian Council on Animal Care and were approved by the Comité de Protection des Animaux du CRCHUQ-UL.

In vivo procedures

Surgery

Parabiosis was performed on 34 female mice at 5 months of age to produce a total of 17 couples. Mice were randomly divided into groups. Negative and positive control groups (e.g. genotype, parabiosis surgery) were included in both surgical cohorts. For each time-point of sacrifice (6, 9, and 12 months post-surgery), groups included one pair of WT/WT and HD/HD mice. Two, four, and five pairs of WT/HD mice were sacrificed at 6, 9, and 12 months post-parabiosis, respectively. Surgeries were performed under aseptic conditions according to previously published protocols [30]. Briefly, mice were anesthetized with 3% isoflurane and maintained on heating pads during the procedure and recovery to prevent loss of body heat. Mirror-image incisions at the flanks of parabiotic pairs were made through the skin. Elbow and knee joints from each parabiont were bound together using 3–0 silk sutures (Covidien Suture, #SS684G), while the skin was attached using 5–0 coated vicryl sutures (Ethicon Suture, #J391H). Each mouse received a subcutaneous injection of lidocaine–bupivacaine (7–3.5 mg/kg) and slow-release buprenorphine (1 mg/kg) prior to surgery as well as a subcutaneous injection of saline after surgery to prevent dehydration. Mice were monitored daily to ensure good overall health and recovery.

Separation of parabionts

In the initial proof of concept experiment, a β-actin GFP mouse was paired with a WT littermate for four weeks and then separated. For separation of the pair, mice were anesthetized with 3% isoflurane and subcutaneously injected with lidocaine–bupivacaine (7–3.5 mg/kg) and slow-release buprenorphine (1 mg/kg). The skin was incised at the site of union to separate the animals. The resulting wound in the corresponding lateral flanks of each mouse was closed with 5–0 coated vicryl sutures (Ethicon Suture, #J391H). Mice were monitored daily and sacrificed one week after separation.

Blood sampling

Submandibular blood withdrawal was performed every 3 weeks under a light and rapid 2% isoflurane anesthesia. The submandibular vein was selected as it was accessible to repeated sampling and sufficiently remote from the surgical site to ensure that blood content was representative of total blood circulation and not biased by proximity to the parabiotic partner. At each collection, ~100 µL of blood was retrieved with a 5 mm lancet (Goldenrod lancet, #NC9891620) and immediately placed in tubes containing acid citrate dextrose (ACD; 0.48% (w/v) $C_6H_8O_7$, 1.32% (w/v) $Na_3C_6H_5O_7$, 1.47% (w/v) $C_6H_{12}O_6$) and Tyrode pH 6.5 (7 mM $NaHCO_3$, 135 mM NaCl, 3 mM KCl, 0.4 mM NaH_2PO_4, 1 mM $MgCl_2$, 4.5 mM Glucose, and 18.7 mM HEPES buffer) to avoid coagulation and activation of platelets.

Hemodynamic measurements

To detect blood pressure and heart rate, we used the BP-2000 Series II hardware system (Visitech Systems, Inc., Apex, NC, USA) according to previously published protocols [31]. Briefly, a platform was set to 34 °C and 20 measurements per mouse were acquired daily between 13h00 and 15h30 using a tail cuff 6.35 mm in diameter and appropriately sized holders. Mice were assessed for 10 consecutive days and the measurements of the first 7 days (the acclimation period) as well as outliers (defined as values $[V] < [Q1 - 1.5 \times \mathrm{IQR}]$ or $> [Q3 + 1.5 \times \mathrm{IQR}]$, where Q stands for quartile and IQR for interquartile range) were excluded from analysis. Mean arterial pressure was calculated from systolic and diastolic blood pressure.

Collection and processing of blood and organ samples

Isolation of blood components

Blood components (erythrocytes, leukocytes, platelets, and plasma) were separated from the same tube by serial centrifugation using an adaptation of previously published protocols [32, 33].

Erythrocytes

Briefly, blood was centrifuged for 4 min at $600 \times g$ at room temperature (RT). The resulting pellet of erythrocytes was washed twice with 0.9% NaCl and stored at −80 °C with a glycerolyte solution (57% $C_3H_8O_3$, 142 mM $C_3H_5NaO_3$, 1 mM KCl, 25 mM Na_3PO_4 pH 6.8) to cryopreserve cells and protect them from lysis. In order to perform western blots, erythrocytes containing glycerolyte were defrosted at RT, 9% NaCl was added drop by drop (one third of the initial volume) and samples were incubated for 10 min at RT. Samples were washed with 2.5% NaCl and centrifuged at $1200 \times g$ for 2 min prior to discarding the supernatant. Pellets were subsequently washed once with 2.5% NaCl and twice with 0.85% NaCl. Pellets were diluted one-to-five with lysis buffer (Pierce, #87788) containing protease and phosphatase inhibitor cocktail 1X final (Thermo Fisher Scientific, #1861284). Protein concentration was measured using a bicinchoninic acid (BCA) protein assay kit (Pierce, #23225) according to the manufacturer instructions.

Leukocytes

Leukocytes were obtained from the buffy coat (the thin layer containing leukocytes lies between the erythrocytes and plasma following a density gradient centrifugation) after incubation with 1X BD (Lysing Buffer, BD Pharm Lyse, #555899) for 15 min and centrifugation at 1500 × *g* for 5 min at RT. The pellet was then solubilized in 25 µL of lysis buffer (Pierce, #87788) containing 1X protease and phosphatase inhibitor cocktail (Thermo Fisher Scientific, #1861284).

Platelets

For platelets, the platelet-rich plasma was collected with the addition of 1/5 volume of ACD, 1/50 volume of 0.5 M ethylenediaminetetraacetic acid (EDTA) pH 8.0 (Fisher BioReagents, #BP2482) and centrifuged twice for 2 min at 400 × *g* and 5 min at 1300 × *g*. The pellet was dissolved in 25 µL of Tyrode pH 6.5, 225 µL of Tyrode pH 7.4, 50 µL of ACD, and 5 µL of 0.5 M EDTA. Platelets were centrifuged for 5 min at 1300 × *g* and the pellet was dissolved in 25 µL of lysis buffer containing 1X protease and phosphatase inhibitor cocktail.

Plasma

Plasma collected during platelet isolation was centrifuged for 15 min at 2500 × *g* at RT. Platelet-free plasma was harvested and stored at −80 °C.

Tissue preparation At sacrifice, mice were anesthetized by intraperitoneal injection (0.1 mL per 10 g of mouse) of 100 mg/kg ketamine and 10 mg/kg xylazine prior to intracardiac perfusion with phosphate-buffered saline (PBS). At dissection, lymph nodes, adipose tissue, lung, kidney, and muscle were obtained from each side of the body, while intestine, spleen, pancreas, heart, and liver were divided as symmetrically as possible. Half of each organ was collected for western blotting and half for immunohistochemistry experiments. In preliminary analyses, several organs including the intestine, heart, lung, spleen, muscle, kidney, and liver were assessed but for complete analysis, we selected two highly vascularized organs, the liver and kidney, and one less vascularized organ, the muscle.

For immunohistochemistry, all organs were collected, post-fixed in 4% paraformaldehyde (PFA) for 48 h and subsequently stored in 20% sucrose in PBS at 4 °C for cryoprotection. At the time of sectioning, brains were cut into 25 µm thick sections using a freezing microtome, while peripheral organs were embedded in a M-1 matrix (ThermoScientific, #1310), frozen and cut into 14 µm (liver) or 10 µm (kidney and muscle) thick sections which were mounted directly onto SuperFrost® slides (Fisher Scientific, #22-037-246). For western blotting, organs were immediately frozen on dry ice and stored at −80 °C. Peripheral organs were homogenized on ice with a dounce homogenizer potter in eight volumes of tris-buffered saline (TBS) containing CompleteTM protease inhibitor cocktail (Roche, #5892970001), 10 µg/ml of pepstatin A (Merck-Millipore, #516481) and phosphatase inhibitor cocktail (Sigma-Aldrich, P5726), as described previously [34]. Brains were homogenized in eight volumes of lysis buffer (150 mM NaCl, 10 mM NaH_2PO_4, 1% Triton X-100, 0.5% sodium dodecyl sulfate (SDS), and 0.5% deoxycholate) containing the same protease and phosphatase inhibitors. After homogenization, all lysates were briefly sonicated (3 × 10 s) and centrifuged at 100,000 × *g* for 20 min at 4 °C to generate a TBS-soluble fraction that contains intracellular (cytosolic) and extracellular proteins. Total protein in cell lysates was then quantified using a BCA Protein Assay Kit (ThermoFisher, #23225). After each soluble fractions' preparation, the insoluble pellet of brain and muscle was homogenized with RIPA buffer (50 mM Tris-HCl pH 8.0, 150 mM NaCl, 5 mM EDTA pH 8.0, 1% NP-40 (IGEPAL), 0.1% SDS, 0.5% deoxycholate) containing Halt Protease Phosphatase Inhibitor 1X (Thermo Scientific, #1861281). Liver and kidney pellets were processed in 1% SDS buffer (20 mM Tris pH 7.4, 1% SDS, 1 mM EDTA, 1X protease inhibitor cocktail (Bimake, #B14001), 1X phosphatase inhibitor cocktail (Sigma-Aldrich, #P5726)). Samples were then sonicated for 2 × 10 s and resuspended with a 26G needle five times. After 30 min on ice, a BCA assay was performed according to the manufacturer's instructions.

Flow cytometry Before immunofluorescent labeling, Fc-receptors were blocked to prevent nonspecific binding using an anti-CD16/CD32 mix (BD Pharmingen, #553142) in potassium phosphate-buffered saline (KPBS) + 1% Fetal Bovine Serum (Sigma-Aldrich, #F1051) for 15 min and peripheral blood mononuclear cells were labeled on ice for 30 min with the fluorescently conjugated primary anti-CD45 v500 antibody (1:100, BD Biosciences, #561487). Erythrocytes were then lysed with a whole blood lysing reagent kit (Beckman Coulter, #6603152) for 20 s and washed with PBS. Data were acquired with a BD LSR II flow cytometer and analyzed with FlowJo software (version 10.0.7; Tree Star). For all analyses, controls containing GFP and v500 only were used to establish gating boundaries [35].

Extraction of RNA and reverse transcription One fourth of the total hippocampus and an equally sized piece of liver and kidney from 12-month parabiosis mice and their associated controls were dissolved in 1 mL of TriReagent™ (Sigma-Aldrich, #T9424). Extraction of RNA was

performed using the Phenol/Chloroform technique, where all centrifugation steps were performed using an Eppendorf Centrifuge 5415R. Briefly, 200 µL of chloroform (Sigma-Aldrich, #C2432) were added per 1 mL of TriReagent™ and mixed vigorously by hand for 30 s. The mixture was left to stand at RT for 2 min prior to centrifugation of samples at 12,000 RPM for 15 min at 4 °C. This step let to division of the solution into two phases. The upper clear phase containing DNA was transferred to a new tube, carefully leaving the DNA-containing interface undisturbed. Next, 500 µL of isopropanol was added (Sigma-Aldrich, #I9516), samples were thoroughly mixed by vortexing and incubated at RT for 10 min. After this incubation, precipitated RNA was collected by centrifugation of samples at 12,000 RPM for 10 min at 4 °C. The supernatant was removed and the RNA pellets were washed by adding 1 mL of 70% ethanol (Greenfield Global, #P016EAAN). RNA pellets were mixed by vortexing and centrifuged at 8000 RPM for 5 min at 4 °C. Supernatants were discarded, and pellets were dried before resuspending in sterile water. To ensure proper solubilization of RNA, samples were heated 10 min at 56 °C. DNAse treatment was performed using 1U of DNAse (Roche, #4716728001) per 1 µg of RNA for 30 min at 37 °C according to manufacturer's instructions. To stop DNase reaction, samples were heated for 10 min at 70 °C with 25 mM of EDTA (Fisher BioReagents, #BP2482-500). RNA samples were reverse-transcribed to cDNA by incubation with 0.5 mM dNTPs (10 mM: Sigma-Aldrich, #11277049001) and 21 ng/µL of random primer (1.6 µg/µL: Sigma-Aldrich, #11034731001) for 5 min at 65 °C. After incubation, samples were placed on ice, MMLV 1X buffer and 10 mM DTT (Invitrogen, #28025-013) was added prior to heating for 2 min at 37 °C. Finally, 200U of MMLV reverse transcriptase (Invitrogen, #28025-013) were added and samples were incubated for 10 min at 25 °C and then 50 min at 37 °C. The reaction was stopped by heating samples for 10 min at 70 °C.

Immunoassays

For all immunoassays, appropriate buffer and secondary antibody controls were included to ensure that all positive staining was due to binding of the primary antibody to the targeted antigen with no contribution from non-specific background or secondary antibody signal.

Erenna Singulex SMC immunoassay

The MW1 polyglutamine and 2B7 N-terminal HTT antibodies were conjugated to magnetic particles (MPs) to a final concentration of 25 µg/mg of MPs for MW1 and 1 µg/µL for 2B7 using the Erenna capture and detection reagent labeling kits from Merck-Millipore, following the manufacturer's instructions (Merck-Millipore, #03-0077-02 and #03-0076-02 respectively). Conjugated/labeled antibodies were diluted in Assay Buffer (Merck-Millipore, #02-0474-00) to 1:1200 and 1:4000 respectively, prior to performing the assay which was carried out using a slightly modified version of previously published protocols [10]. Briefly, mouse plasma samples were pre-diluted 1:10 in complete artificial CSF and 2B7 antibody coupled, to MPs, was added to assay buffer containing 6% bovine serum albumin (BSA, w/v, Bioshop, #ALB001), 0.8% Triton X-100 (v/v, Sigma-Aldrich, #T8787), 750 mM NaCl and complete protease inhibitor in a 96-conical assay plate (Axygen, # P-96-450V-C). The plate was sealed and incubated on a shaker at RT for 1 h. Samples were washed on a magnetic rack using a HydroFlex Microplate 8 Channel Washer (Tecan), in 1X Erenna Wash Buffer (Merck-Millipore, #02-0111-03). After washing, MPs were incubated with MW1 detection antibody for 1 h at RT. Samples were again washed in 1X Erenna Wash Buffer on a magnetic rack in a HydroFlex washer. The antibody-antigen complex was transferred to a new 96-conical assay plate to eliminate nonspecific binding to the plastic. After buffer aspiration, Elution Buffer B (Merck-Millipore, #02-0297-00) was added to the plate for 5 min of incubation while shaking. The eluted detection antibody was transferred to a Nunc 384-well analysis plate (Sigma-Aldrich, #264573) and neutralized with Buffer D (Merck-Millipore, #02-0368-00). The analysis plate was spun down to eliminate foaming and bubble formation, sealed, and subsequently analyzed with the Erenna Immunoassay System (Merck-Millipore).

Quantification of inflammatory markers

Concentrations of cytokines were determined in plasma, liver and kidney using the Q-Plex™ Mouse Cytokine (16-Plex) Kit (Quansys Biosciences, #110349MS). This Q-Plex analysis was performed according to the manufacturer's instructions. Absorbance values were measured at 450 nm using a myECL imager (ThermoFisher, #G2236X).

Protein electrophoresis and western blotting

For standard western blots, 30 µg of proteins were run on a 10% SDS-polyacrylamide gel at 100 V until the dye migrated out of the gel. After migration, proteins were transferred onto Amersham Hybond 0.45 µm polyvinylidene difluoride membranes (GE Healthcare, #10600023) in Towbin buffer with 20% methanol at 130 V for 1 h. Membranes were removed from the transfer, blocked for 1 h in 0.5% BSA and 5% milk powder in PBS containing 0.1% Tween 20 (PBST) and incubated overnight (O/N) in primary antibody in the same blocking buffer. Secondary antibodies were horseradish peroxidase (HRP)

conjugated. HRP signal was revealed in chemiluminescence with Immobilon Forte Western HRP Substrate (Merck-Millipore, #WBLUF0500) using a myECL imager (ThermoFisher, #G2236X). Where the Odyssey imaging system was the detection method, REVERT total protein stain (LI-COR Biotechnology, #926-11011) was performed according to the manufacturer's instructions.

The detailed specification for each western blot have been summarized in the Supplementary material and methods (Tables S1 and S2).

Filter retardation assay

The filter retardation assay was performed in triplicate with 5 µg of tissue pellet homogenate diluted in PBS to complete a volume of 70 µL to which 30 µL of SDS/Dithiothreitol (DTT) mix was added (final concentration 2% SDS and 100 mM DTT). Samples were boiled at 100 °C for 5 min and cooled to RT. A cellulose acetate membrane (Steriltech, #1480025) was washed 2 × 5 min in 1% SDS in PBS prior to loading. Once the apparatus was assembled (HYBRI DOT Manifold, #1050MM), 100 µL of each sample was loaded per well and vacuum filtered through the membrane. Following filtration, the membrane was washed with 0.1% SDS in PBS, removed from the equipment, dried for 30 min and washed 3 × 5 min with 0.1% SDS and rinsed once with PBS to remove excess SDS. The membrane was then blocked with 5% BSA in PBS for 1 h at RT and incubated with an anti-HTT clone EM48 antibody and anti-total HTT N18 antibody (kindly provided by Dr. Ray Truant, McMaster University, Canada) in 5% BSA in PBST O/N at 4 °C. Incubation in Li-Cor secondaries was performed for 45 min and membranes were visualized using the Odyssey CLx imaging system (Odyssey; Li-Cor).

FRASE assay

The quantification of seeding-competent HTT species in cortex homogenates was performed as previously described [24]. In brief, frozen cortex tissue was homogenized in 10-fold excess (w/v) of ice-cold 10 mM Tris-HCl pH 7.4, 0.8 M NaCl, 1 mM EDTA, 10% sucrose, 0.25 U/µL benzonase and complete protease inhibitor cocktail (Roche, #5056489001) with a dounce homogenizer. The homogenate was incubated for 1 h at 4 °C on a rotating wheel and centrifuged for 20 min at 2700 × *g* (4 °C) to remove cell debris. Next, cortex homogenates (5 µg total protein/replicate) were added to the aggregation reaction of recombinant sensor proteins, two soluble glutathione S-transferase (GST) HTT exon-1 (HTTex1) fusion proteins with 48 glutamines C-terminally fused to CyPet or YPet (1.2 µM GST-Ex1Q48-CyPet and GST-Ex1Q48-YPet in 50 mM Tris-HCl pH 7.4, 150 mM NaCl, 1 mM EDTA, 1 mM DTT and 14 U PreScission Protease (GE Healthcare, #27-0843-01) per nmol sensor proteins). To monitor the aggregation of sensor proteins, fluorescence signals were measured every 20 min following a 5 s pulse of vertical shaking with a Tecan M200 fluorescence plate reader at 25 °C for 30 h (CyPet donor fluorescence at excitation (Ex): 435 nm/emission (Em): 475 nm; YPet acceptor fluorescence at Ex: 500 nm/Em: 530 nm; FRET channel (DA) was recorded at Ex: 435 nm/Em: 530 nm). FRET efficiency E (in%) was calculated as follows: E = (DA-cDxDD-cAxAA)/AA with DD = donor channel signal, AA = acceptor channel signal, cD = donor bleed-through and cA = acceptor cross excitation. Seeding effects (Δt50 [h]) were quantified by subtracting the t50 values (time at half-maximal FRET efficiency) of the respective sample from the negative control. To obtain the t50 values, the aggregation kinetics were curve fitted by Richard's five-parameter dose–response curve using GraphPad Prism.

$$y = y_0 + \left(\frac{y_\infty - y_0}{1 + 10^{((Logxb - x) \times HillSlope)^S}}\right)$$

Immunohistochemistry

Detection of mHTT aggregates in peripheral organs After tissue processing, sections were immunoperoxidase stained with the HTT antibody S829 (kindly provided by Dr. Gillian Bates, University College London, United Kingdom). Briefly, sections were rinsed in 0.1 M Tris-HCl pH 7.5 with 0.9% NaCl (TBS) followed by antigen retrieval with citrate buffer pH 6.2 for 30 min at 90 °C. After the tissue was cooled, endogenous biotin was blocked using a 3% hydrogen peroxide solution (H_2O_2) and sections were incubated in primary antibody (S829, 1:2000) diluted in blocking solution (TBS, 2% Horse serum (Vector Laboratories, #S-2000) and 0.1% Triton™ X-100) O/N at RT. Sections were then incubated for 1 h at RT in biotinylated horse anti-goat secondary antibody (1:500, Vector Laboratories, #BA9500) in blocking solution, followed by incubation with avidin-biotin peroxidase complex (ABC-HRP complex) using the Vectastain Elite ABC kit (Vector Laboratories, #PK-6100), as recommended by the manufacturer. The signal was revealed with 3,3-diaminobezidine (DAB, Sigma-Aldrich, #D5905) in 0.1 M Tris-HCl pH 7.5. Finally, sections were rinsed in water and counterstained in eosin (Sigma-Aldrich, #HT110116). They were then dehydrated in ascending grades of ethanol, cleaned in Citrisolv (Decon Laboratories, #1601) and coverslipped with DPX mounting media (Electron Microscopy Sciences, #13512).

Detection of mHTT aggregates in CNS Free-floating sections were rinsed in 0.2 M PBS, placed in 3% H_2O_2 for

30 min and blocked with 4% normal goat serum (NGS, Wisent Bioproducts, #053-150), 0.4% Triton™ X-100 and 1% BSA. Sections were then incubated O/N at 4 °C with anti-HTT clone EM48 (1:500, Merck-Millipore, #MAB5374) in blocking buffer. After primary antibody incubation, samples were washed 3 × 8 min in 0.2 M PBS and incubated for 1 h at RT in biotinylated goat anti-mouse secondary antibody (1:1500, Vector Laboratories, #BA9200) diluted in blocking solution and washes were repeated. After PBS washes, brain slices were placed in ABC-HRP complex solution (Vector Laboratories, # PK-6100), as recommended by the manufacturer. Following washes in acetate imidazole 0.2 M pH 7.2, the sections were revealed with DAB (Sigma-Aldrich, #D5905) mixed with 2.6% $NiSO_4$ to enhance signal. Sections were mounted on SuperFrost® slides (Fisher Scientific, #22-037-246), rinsed in water and counterstained with 0.5% methyl-green (Sigma-Aldrich, #323829) in 0.1 M sodium acetate pH 4.2. Slides were dehydrated and cover-slipped in the same manner as described for peripheral organs.

Detection of neurons and microglia in the striatum and cortex Free-floating sections were rinsed in 0.1 M PBS, placed in 3% H_2O_2 for 30 min and blocked with 5% NGS (Wisent Bioproducts, #053-150) and 0.1% Triton X-100 in PBS 0.1 M. Sections were then incubated O/N at 4 °C with one of the following antibodies in blocking buffer; anti-Iba1 (1:1000, Wako, #019-19741), anti-calbindin (1:1000, Sigma-Aldrich, #C9848) or anti-DARPP32 (1:1000, Cell signaling, #2306S). After primary antibody incubation, samples were washed 3 × 8 min in 0.1 M PBS and incubated for 1 h at RT in either biotinylated goat anti-mouse secondary antibody (1:1500, Vector Laboratories, #BA9200) or biotinylated goat anti-rabbit secondary antibody (1:1500, Vector Laboratories, #BA1000) diluted in blocking solution and washes were repeated. After PBS washes, brain slices were placed in ABC-HRP complex solution (Vector Laboratories, # PK-6100), as recommended by the manufacturer. Following washes in Tris 0.05 M pH 7.6, the sections were revealed with DAB (Sigma-Aldrich, #D5905). Sections were mounted on slides and air-dried prior to dehydration and coverslipping.

Evaluation of blood vessel permeability Slices were washed in 0.1 M PBS and post-fixed in 4% PFA pH 7.4 for 1 h. They were put in 3% H_2O_2 for 30 min and incubated in a blocking solution of 5% NGS (Wisent Bioproducts, #053-150) and 0.1% Triton™ X-100 in 0.1 M PBS for 30 min. They were subsequently incubated with Immunoglobulin G (IgG) antibody (biotinylated goat anti-mouse IgG, 1:500, Vector Laboratories, #BA-9200) in blocking solution for 45 min and placed in a solution containing ABC-HRP complex (Vectastain Elite ABC kit; Vector Laboratories, #PK-6100) for 45 min. The bound antibodies were visualized by placing the sections in a 0.05 M Tris buffer solution containing 0.5 mg/ml of DAB (Sigma-Aldrich, #D5905) and 0.1% of 30% H_2O_2 (Sigma-Aldrich, #H1009). Sections were mounted on slides and air-dried prior to dehydration and coverslipping.

Immunofluorescence

Sections were rinsed three times in KPBS and an antigen retrieval step with citrate buffer pH 6.2 for 30 min at 80 °C was performed. Sections were then washed 3 × 5 min in KPBS, blocked in 0.5% BSA, 0.4% Triton™ X-100 and 10% normal donkey serum (Sigma-Aldrich, #D9663) in KPBS for 30 min and incubated with Collagen IV (1:500, Merck-Millipore, #AB769) primary antibody diluted in blocking solution O/N at 4 °C. The next morning, sections were washed in KPBS and incubated with donkey anti-goat Alexa Fluor 488 conjugated (Invitrogen, #A-11055) secondary antibody at 1:500 in blocking solution for 2 h at RT. After rinsing, sections were incubated in KPBS containing 0.022% 4′,6-diamidino-2-phenylindole (DAPI, Molecular Probes, #D3571) for 7 min, washed and mounted on SuperFrost® slides (Fisher Scientific, #22-037-246). After completing mounting, slides were placed in 70% ethanol, covered with autofluorescence eliminator reagent (Merck-Millipore, #2160) for 5 min prior to washing in 70% ethanol three times and coverslipping with Fluoromount-G.

Quantitative reverse transcription polymerase chain reaction

Reverse transcription quantitative polymerase chain reaction (RT-qPCR) using Master Mix SybrGreenER (Thermofisher, #11762100) was performed in the Corbett Rotor Gene RG-3000. The following primers were used: murine *glyceraldehyde 3-phosphate dehydrogenase* (*gapdh*) forward GAACATCATCCCTGCATCCA and reverse CCAG TGAGCTTCCCGTTCA; *WT HTT*: forward CAGGTCC GGCAGAGGAACC and reverse TTCACACGGTCTTTC TTGGTGG; *mHTT*: forward GCCCGGCTGTGGCTGA and reverse TTCACACGGTCTTTCTTGGTGG. PCR efficiency (E) and coefficients of determination (R^2) for each primer were validated using five serial 2-fold dilution points where Ct(s) were plotted versus the logarithm of dilution according to previous publication: [36] *gapdh* primers $E = 105\%$, $R^2 = 0.915$; *WT HTT* primers $E = 105\%$ $R^2 = 0.957$; *mHTT* primers $E = 109\%$ $R^2 = 0.978$. The RT-qPCR reaction consisted of 10 µL Master Mix SybrGreener, 1 µL of each primer, 6 µL of sterile water and 2 µL of previously prepared cDNA (cDNA hippocampus = 40 ng/µL; cDNA liver and kidney = 120 ng/µL). Samples were amplified according to the following program: initial

denaturation for 10 min at 95 °C, followed by 40 cycles of 15 s at 95 °C and 60 s at 59 °C. Subsequently, a dissociation curve (melting curve) analysis was applied with one cycle at 95 °C for 15 s, 60 °C for 1 min and 0.5 °C ramp rate to 95 °C to confirm specific amplification. Minus reverse transcription or water controls were included in each run and uniformly displayed a lack of signal. Analysis of relative gene expression data were performed using the $2-^{\Delta\Delta CT}$ method, as previously described[37], using *gapdh* as the reference gene. All PCR analyses were carried out under RNase/DNase-free conditions.

Quantification and analysis

Western blots

Immunoblot band intensity was evaluated with either ImageJ Analysis Software (National Institutes of Health, http://imagej.nih.gov.acces.bibl.ulaval.ca/ij) or the Odyssey Imaging System (Odyssey; Li-Cor, Lincoln, NE). Protein signals were corrected to GAPDH, Vinculin or REVERT signal intensity to control for differences in loading. To normalize samples run on separate gels, all data is shown as % of non-parabiotic controls.

Stereological counts

Stereology was performed using the Optical Fractionator probe (Stereo Investigator, Microbrightfield) installed on an E800 Nikon microscope in order to count mHTT positive aggregates in the periphery and relevant neuronal and glial populations in the brain. Perimeters of the peripheral organs and brain structures were outlined under a 2× or 4× objective lens respectively, using the tracing contour option. Counts in the periphery were performed by a blinded investigator under a 60× objective lens within the defined perimeter every 14th (liver), 12th (kidney), or 10th (muscle) section in a series of S829-stained sections throughout the entire organ of each mouse. In the periphery, the counting frame was set to 75 × 75 with a grid layout of 500 × 500 for the kidney and 750 × 750 for the liver and the muscle. For counts in the brain, two independent blinded investigators counted every 10th section for a total of three striatal and three cortical sections. The counting frame was set to 100 × 100 and the grid layout to 300 × 300, to count between 100 and 120 squares per structure using a 20× objective lens.

Vascular abnormalities

Angiopathy and leakage were quantified in mice sacrificed 12 months post-surgery. For angiopathy, three slices of the cortex and striatum equally distributed along the rostro-caudal axis were selected. For leakage, three consecutive brain slices from the widest part of the striatum separated by 250 µm (~0.50; 0.25 and 0.00 mm from bregma) were analyzed. To evaluate angiopathy, we acquired one picture of a fixed size (606 × 606 µm) in both the cortex and striatum using an Imager Z.2 AXI0 confocal microscope (Zeiss, Oberkochen, Germany). Fiji (version 2.0) software was used to calculate signal intensity, for both leakage and angiopathy, which was then averaged to obtain a mean intensity value for each image. To assess Feret diameter, density and area fraction of the blood vessels, the "analyze particles" tool was used. From the diameter measurements, we divided the population of blood vessels into two subpopulations: blood vessels with a diameter above and below 10 µm. The branch number and length was calculated using the Fiji (version 2.0) plug-in "analyze skeleton" according to previously published protocols [38]. Briefly, the binary image was skeletonized and subsequently analyzed with the aforementioned plug-in. To measure the amount of IgG in the parenchyma, photomicrographs were taken using Picture Frame software (Microbrightfield, Williston, VT) linked to an E800 Nikon microscope (Nikon Instruments, Melville, NY). Pictures were subsequently transformed into binary images and the percentage of staining within the area of interest was calculated using the "area fraction" tool in Fiji (version 2.0).

Statistical analysis

Animals underwent surgery in two distinct batches, with processing and data collection also conducted separately. All data were reproducible between both individual animals and batches. No sample size calculations were performed as animal numbers needed to be kept to a minimum due to the tight ethical regulation surrounding the parabiosis paradigm. Prior to commencing our data analysis, an outlier was defined as a data point more than 1.5 interquartile ranges below the first quartile, or 1.5 interquartile ranges above the third quartile. Two-way ANOVAs followed by Tukey's or Sidak's post-hoc tests were used for all analyses of multiple groups (genotype of the mouse of interest vs. genotype of the partner) at a single time-point. When unequal variances were detected between groups, or when the data did not have a normal distribution, the statistical analysis was modified according to the type of data being analyzed. For two-way ANOVA analyses with unequal variance, each genotype was isolated and assessed by one-way ANOVA with Holm–Sidak's post-hoc tests or an unpaired *t*-test depending on the number of groups. For one-way ANOVA analyses, Kruskal–Wallis with Dunn post-hoc tests were performed when analyzing the effect of the partner genotype—referred to as treatment effect throughout the text—on the mouse of interest at a specific time point. Mann–Whitney tests were used when comparing two

groups at a single time point. All data are shown as the mean ± SEM. Statistical significance was set at $p < 0.05$. All statistical analyses were performed using Prism (6.0c; Graph-Pad Software Inc., La Jolla, CA). The *Service de Consultation Statistique de l"Université Laval* (Québec, Québec, Canada) was also consulted for some of the statistical analyses.

Results

To test the capacity of circulating blood to disseminate mHTT to various organs, we opted for the use of parabiosis, an approach which consists of surgically connecting two animals by their flank to create anastomosis of blood vessels. As a proof of concept, we first performed a study in which we surgically connected a GFP-expressing mouse to a WT littermate for four weeks. At the end of the four weeks, the mice were separated. Blood sampling was performed at day 5 and at separation (Fig. S1a). GFP^+ leukocytes, analyzed by flow cytometry (Fig. S1b), were found to be present in equal number to non-fluorescent leukocytes at both time points. These experiments confirmed that the parabiosis procedure allowed efficient transfer of blood cells between paired mice and that these cells could be identified in the circulation of either animal.

Having established the efficacy of the surgical procedure, experiments were conducted using the zQ175 mouse line that expresses a chimeric *mHTT* gene with human exon 1 at endogenous levels [29]. Experimental groups were generated from the same WT/HD pair. Depending on the genotype of the mouse being analyzed, the groups were referred to as either $WT^{(HD)}$ or $HD^{(WT)}$. The controls included WT and HD parabionts ($WT^{(WT)}$ and $HD^{(HD)}$) and non-parabionts ($WT^{(NP)}$ and $HD^{(NP)}$). To understand the time required for detection of mHTT in the circulation and organs of the parabionts, blood was collected starting 3 days post-surgery and pairs were sacrificed at 6, 9, and 12 months post-surgery (Fig. 1a). To confirm the transfer of mHTT between mice, the presence of mHTT within all types of blood cells-erythrocytes, leukocytes and platelets-as well as plasma (Fig. 1b-e) was measured by western blot and Singulex assay, respectively. By day 3 post-surgery, mHTT could be detected in both $WT^{(HD)}$ and $HD^{(WT)}$ mice. From day 7 onward, the number of mHTT containing erythrocytes was similar in both groups (Fig. 1b), as were the number of mHTT-containing leukocytes (Fig. 1c) and platelets (Fig. 1d). Furthermore, mHTT was detected in the plasma of $WT^{(HD)}$ mice at both 6 and 12 months but not in WT mice that did not undergo parabiosis (Fig. 1e), indicating the efficacy of the procedure. We then began assessment of peripheral organs by selecting two highly vascularized organs, the liver and kidney, and one less vascularized tissue, the muscle. The soleus muscle of the leg was chosen as it is characterized by a particularly high number of mitochondria making it more susceptible to oxidative stress. Western blot analysis of WT HTT and mHTT showed that parabiosis neither resulted in detectable levels of mHTT in WT mice nor affected the levels of WT HTT in any of the organs evaluated 12 months post-surgery (Fig. 1f–h). However, in the kidney, mHTT was reduced in both parabiosis groups as compared with the non-parabiosis HD controls (Fig. 1g) indicating that the parabiosis procedure itself could impact mHTT levels.

While soluble mHTT is clearly present in both blood cells and plasma, it is not necessarily the most likely form to accumulate in organs. We therefore also assessed insoluble mHTT using filter retardation assay and immunohistochemistry. No accumulation of mHTT aggregates was observed in $WT^{(HD)}$ mice at any time point in the liver (Fig. S2a), kidney (Fig. S2b) or muscle (Fig. S2c) when measured using the filter retardation assay. However, this assay did not differentiate between $HD^{(NP)}$ and $WT^{(NP)}$ and only demonstrated a significant genotype effect in the kidney (Fig. S2b). The absence of differences suggests that the large SDS-insoluble aggregates measured using this method are not present in peripheral organs. In contrast, mHTT aggregates were detectable by immunohistochemistry as early as 6 months post-surgery in the liver (Fig. 2a), kidney (Fig. 2b) and muscle (Fig. 2c) of $WT^{(HD)}$ mice. In all organs, a certified pathologist confirmed the presence of aggregates within cells and further specified the cell types as hepatocytes and tubular cells of the liver and kidney, respectively. In the muscle, aggregates were determined to be present within myocytes, generally in the nuclei. Nine and 12 months post-surgery, $HD^{(WT)}$ mice showed fewer aggregates in the liver than $HD^{(HD)}$ (Fig. 2d). In the kidney, both parabiosis groups, $HD^{(WT)}$ and $HD^{(HD)}$, had less aggregates than age-matched mice that did not undergo parabiosis (Fig. 2e). Analysis of the muscle did not reveal group differences (Fig. 2f). The consistency of the soluble and insoluble mHTT decrease after parabiosis in the kidney suggests that both changes may be mediated by the same mechanism. For this reason, *HTT* and *mHTT* mRNA levels were quantified in the kidney and the liver. In the liver, parabiosis with WT mice led to increased expression of both *HTT* and *mHTT* in $HD^{(WT)}$ mice although mHTT aggregates were reduced in this tissue (Fig. S2d). In the kidney, no genotype or group effects were present for HTT indicating that any changes in protein level was likely due to increased protein degradation. An interesting additional finding was the presence of *mHTT* RNA in $WT^{(HD)}$ mice despite the absence of detectable soluble protein (Fig. S2e). *mHTT* RNA has previously been found to be present in blood cells [39] and it is therefore likely that such cells were the source of *mHTT* in this organ. The increased sensitivity

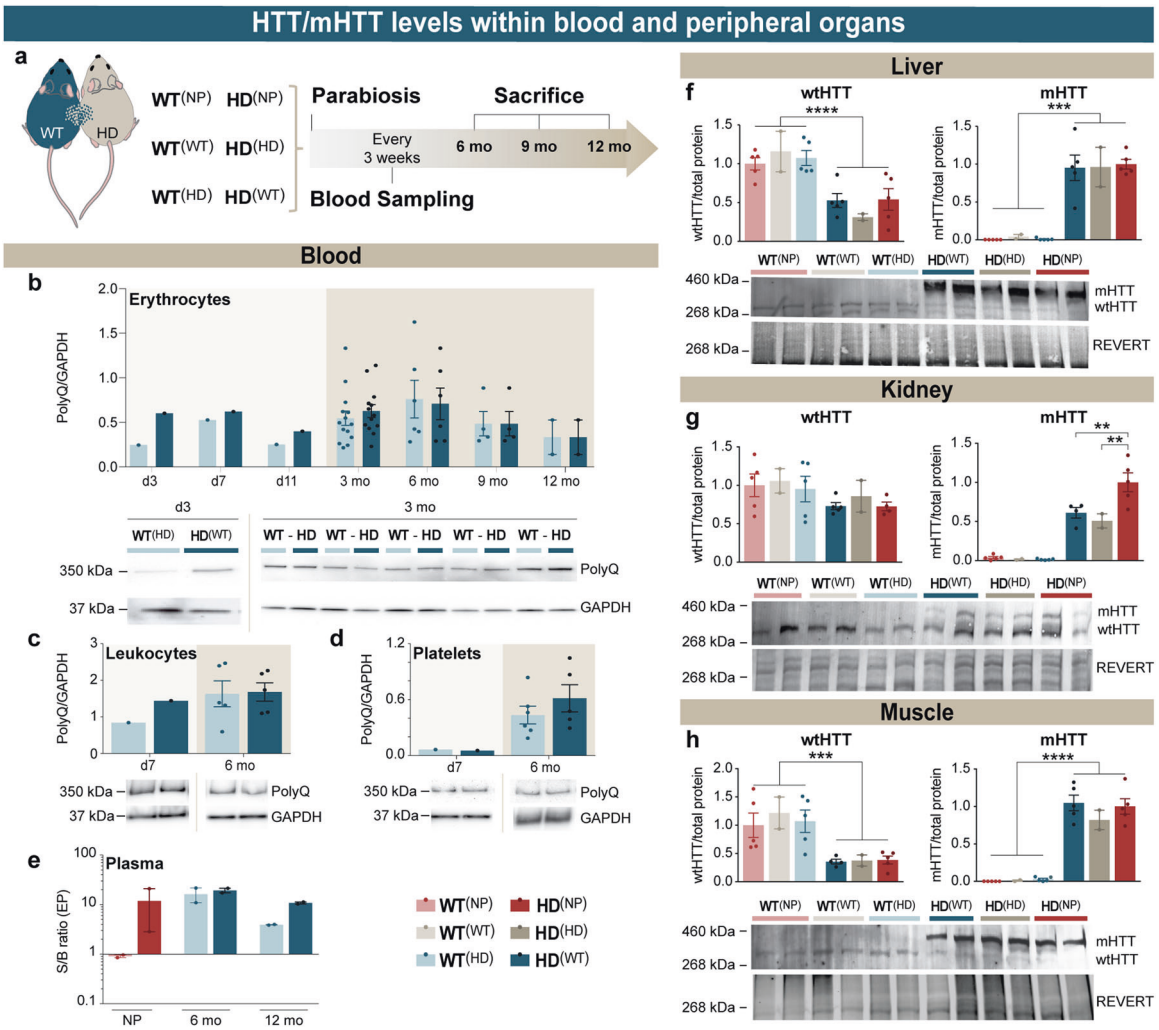

Fig. 1 HTT/mHTT levels in blood and peripheral organs of parabionts. **a** Following parabiosis surgery, blood samples were collected every 3 weeks and pairs of mice were periodically sacrificed between 6 and 12 months. The presence of mHTT was evaluated within **b** erythrocytes, **c** leukocytes, **d** platelets and **e** plasma at the indicated time points. HTT/mHTT protein content in **f** liver, **g** kidney, and **h** muscle was quantified by western blot at 12 months post-surgery ($n = 2$ for same genotype pairs and n=5 for multi-genotype pairs). Data are expressed as mean ± SEM with data points indicating values for each animal. Statistical analyses were performed using **b** a three-way ANOVA or **c–h** two-way ANOVA with Tukey's or Sidak's post-hoc tests. $^{**}p < 0.01$; $^{***}p < 0.001$; $^{****}p < 0.0001$. d day, EP event photons, GAPDH Glyceraldehyde 3-phosphate dehydrogenase, HD Huntington's disease, HTT huntingtin protein, kDa kilodalton, m mutant, mo month, NP non-parabiotic mice, PolyQ polyglutamine stretch of mHTT protein, S/B ratio signal/background ratio, WT wild-type.

of RT-qPCR as compared with western blotting could explain the detection of *mHTT* mRNA in the absence of soluble mHTT protein, or the mRNA may have been present but not transcribed.

Having observed the presence of mHTT protein and mRNA in WT mice, peripheral organs were evaluated for features of cellular stress. Given the predominance of mitochondrial dysfunction in HD patients, the levels of translocase of the outer membrane 40 (TOM40) and cytochrome c were evaluated. TOM40 is an outer membrane transport protein that has previously been shown to be decreased in mouse models of HD; [40] a decrease that has been linked to increased cytochrome c release and apoptosis [41]. In the liver, no difference in TOM40 was observed between groups (Fig. 3a), but for cytochrome c, there was a main effect of interaction between genotype and treatment ($F_{2,14} = 4.818$, $p = 0.026$) (Fig. 3b), with a trend towards increased levels of cytochrome c in $HD^{(NP)}$ mice as compared with $WT^{(NP)}$, which was absent in $HD^{(WT)}$ (Fig. 3b). In the kidney, there was an overall effect of genotype and treatment on the amount of protein detected (Genotype: $F_{1,13} = 34.29$, $p < 0.0001$; Treatment: $F_{2,13} = 3.960$, $p = 0.0454$) with $HD^{(NP)}$ showing higher levels than $WT^{(NP)}$ (Fig. 3c). This increase was absent in $HD^{(WT)}$ mice which did not significantly differ from WT controls (Fig. 3c). Similar genotype and treatment effects were observed for

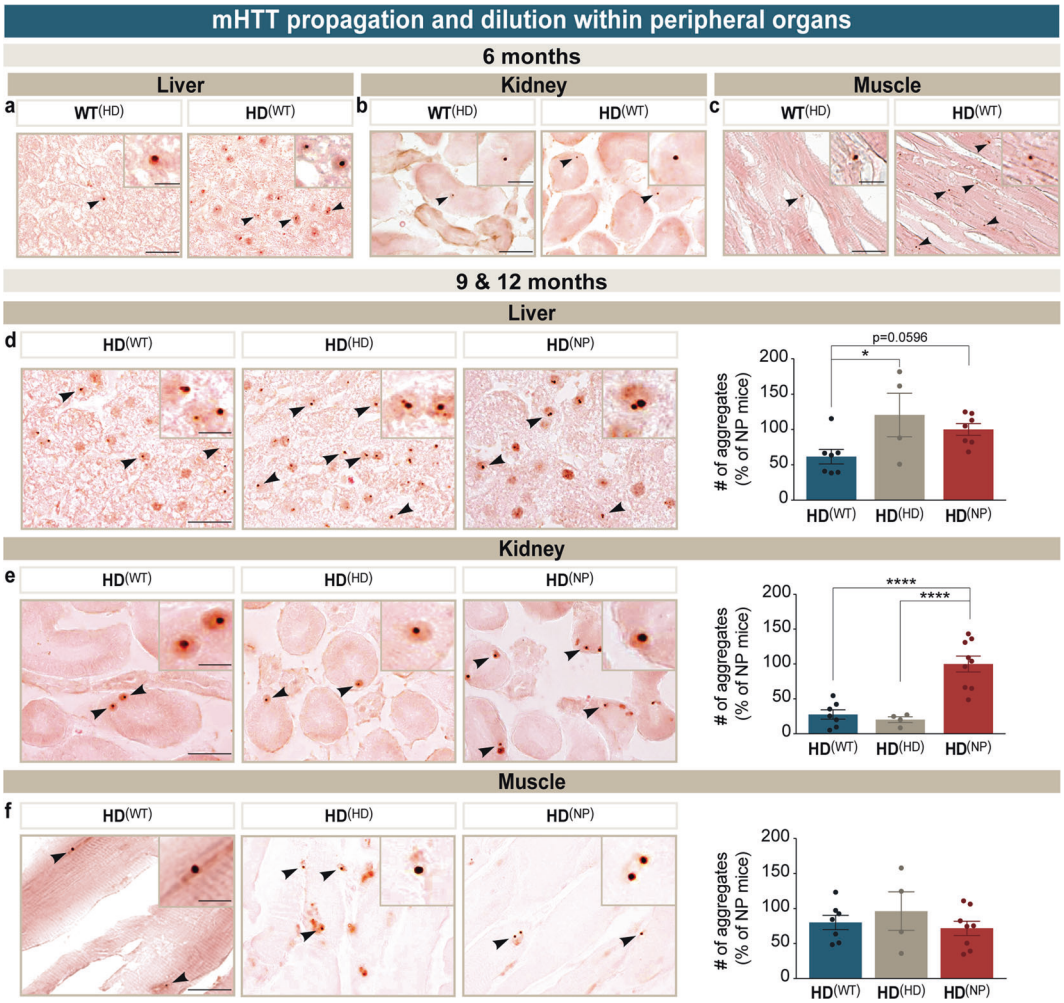

Fig. 2 mHTT propagation and dilution in peripheral organs of parabionts. a Liver, **b** kidney and **c** muscle from parabiotic pairs were assessed for the presence of mHTT aggregates using immunohistochemistry at 6 months post-surgery. Representative photomicrographs and quantifications of stereology are shown for $HD^{(WT)}$ mice and controls in **d** liver, **e** kidney, and **f** muscle at 9 and 12 months post-surgery. mHTT aggregates are indicated by arrowheads. Insets depict an optical magnification of the identified aggregates. Scale bars = 50 µm, inset = 12.5 µm. Data are expressed as mean ± SEM with data points indicating values for each animal. $N = 4$ for same genotype pairs and $n = 9$ for multi-genotype pairs. Statistical analyses were performed using a one-way ANOVA followed by Holm–Sidak's post-hoc tests. $^{*}p < 0.05$; $^{****}p < 0.0001$. HD Huntington's disease, HTT huntingtin protein, m mutant, NP non-parabiotic mice, WT wild-type.

cytochrome c (Genotype: $F_{1,13} = 6.406$, $p = 0.0251$; Treatment: $F_{2,13} = 15.81$, $p = 0.0003$) (Fig. 3d) with a striking effect of parabiosis in both WT and HD mice; all parabiotic mice showing lower levels of cytochrome c than the non-parabiotic controls. While the TOM40 data was unexpected and differed from previously published reports, the cytochrome c data in the kidney and liver corroborates the changes in insoluble mHTT levels and suggests that the reduction of mHTT may contribute to the decrease in cytochrome c. In the muscle, the TOM40 levels were more consistent with previous reports [40] as there was an overall decrease in HD mice (Genotype: $F_{1,14} = 37.97$, $p < 0.0001$) (Fig. 3e). Importantly, this genotype effect was diminished in $HD^{(WT)}$ when compared with $HD^{(HD)}$ mice using a *t*-test ($p = 0.032$) (Fig. 3e). Consistent with the lack of changes of insoluble mHTT in the muscle, no group differences were detected for cytochrome c in this tissue (Fig. 3f).

After establishing the presence of changes in the periphery, we shifted our focus to the vasculature as it is an important connection between the periphery and the CNS. The vasculature of the striatum and cortex, the primarily targeted brain structures in HD [14], were therefore evaluated for changes (Figs. 4 and S3). For this assessment, Collagen IV, as part of the basement membrane, was selected as a marker of normal vascular structure as previous publications have shown that cerebral amyloid angiopathy is measurable with this label [42, 43]. In the cortex, no differences in signal intensity of Collagen IV were distinguished between any experimental groups at the latest time point (Fig. S3a). In the striatum at 12 months

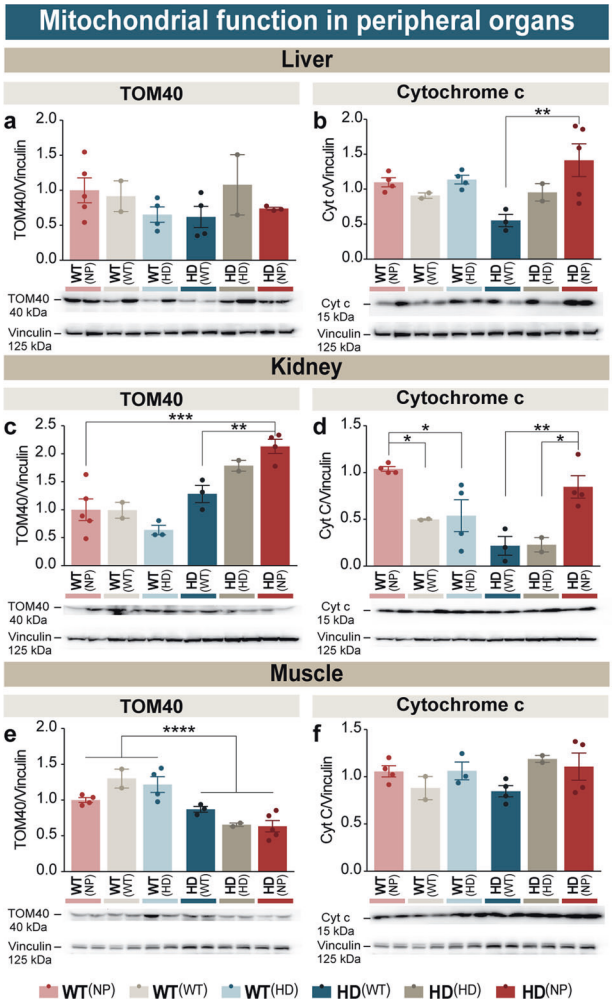

Fig. 3 Mitochondrial function in peripheral organs of parabionts. Quantifications and immunoblots of mitochondrial proteins TOM40 and Cytochrome c 9 months post-parabiosis for **a**, **b** liver, **c**, **d** kidney, and **e**, **f** muscle. Data are expressed as mean ± SEM with data points indicating values for each animal. $N = 2$ for same genotype pairs and $n = 5$ for multi-genotype pairs. Statistical analyses were performed using a two-way ANOVA with Tukey's or Sidak's post-hoc tests. $*p < 0.05$; $**p < 0.01$; $***p < 0.001$; $****p < 0.0001$. Cyt c cytochrome c, HD Huntington's disease, kDa kilodalton, NP non-parabiotic mice, TOM40 translocase of the mitochondrial outer membrane 40, WT wild-type.

post-parabiosis, Collagen IV intensity was significantly higher in $WT^{(WT)}$ mice than in any other experimental group, including $WT^{(HD)}$ (Fig. 4a). Since an increase in signal intensity of Collagen IV with age is a physiological process [44], this is indicative of pathological changes in $WT^{(HD)}$ mice. This interpretation is further strengthened by the presence of differences between $WT^{(WT)}$ and $HD^{(HD)}$ mice which are consistent with previously published reports of vascular changes in mouse models of HD, as well as in patients [45]. One of the previously reported changes in vasculature in HD patients is an increased density of vessels [45]. To determine if the decrease in Collagen IV signal intensity was secondary to a change in vessel number, we evaluated the density and the area covered by Collagen IV^{+} structures (Figs. 4b, c and S3b, c). However, neither parameter was altered suggesting that the changes in signal intensity likely reflect reductions in protein expression.

While the density of blood vessels has been reported to increase in patients, additional structural changes, such as decreased diameter and altered morphology of branches, have been reported in the R6/2 transgenic mouse model of HD [45]. Therefore, we assessed other structural parameters and found that vessel diameter (Fig. S3d) and population percentage (Fig. S3e) as well as number of vessel branches (Fig. S3f) and branch length (Fig. S3g) showed genotype or interaction effects in the cortex (Fig. S3h) (diameter-Genotype: $F_{1,8} = 5.441$, $p = 0.0480$; populations by diameter-Genotype: $F_{1,8} = 9.007$, $p = 0.0170$; branching-Interaction: $F_{1,7} = 8.302$, $p = 0.0236$; branch length-Interaction: $F_{1,8} = 12.08$, $p = 0.0084$). No genotype specific changes were observed for any of these parameters in the striatum (diameter-Genotype: $F_{1,8} = 1.620$, $p = 0.2388$; populations by diameter-Genotype: $F_{1,8} = 0.6476$, $p = 0.4442$; branching-Genotype: $F_{1,8} = 2.051$, $p = 0.1900$; branch length-Interaction: $F_{1,8} = 15.64$, $p = 0.0042$) (Fig. 4d–h). For all analyses, the exact parameter measured is pictorially represented (Figs. 4i and S3i). In the cortex, parabiotic-partner equally influenced the vessel morphology with $WT^{(HD)}$ mice displaying a phenotype that was partway between $WT^{(WT)}$ and

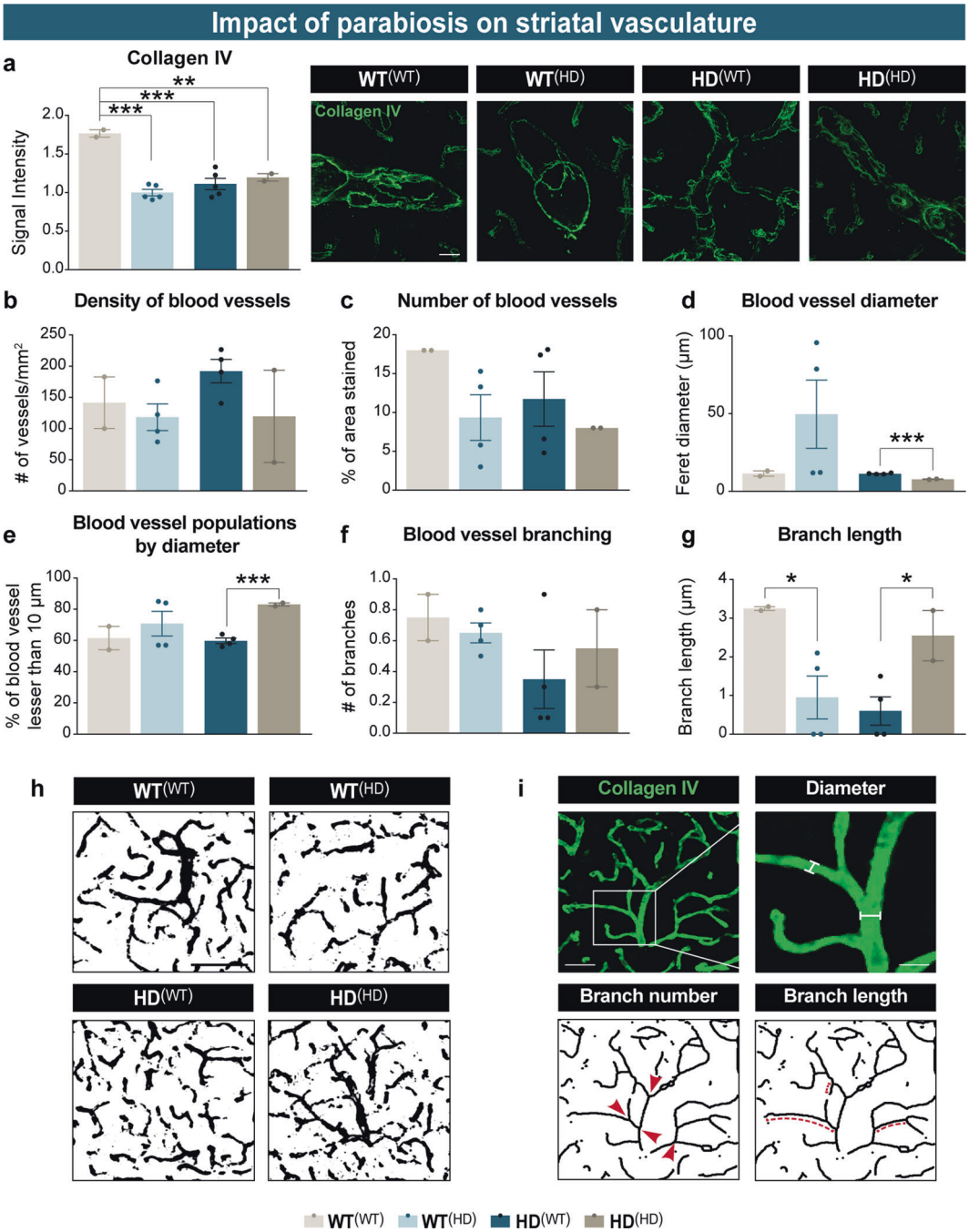

Fig. 4 Impact of parabiosis on striatal vasculature in parabionts. **a** Quantification and representative images of mean fluorescence intensity for Collagen IV at 12 months post-surgery. **b** Density, **c** number, **d** diameter and **e** vessel population by diameter were assessed as well as **f** branching and **g** branch length. **h** Representative images of striatal vasculature and **i** depiction of quantification methods. Scale bars = **a** 25 µm, **h–i** 40 µm, **i**, high magnification 20 µm. Data are expressed as mean ± SEM with data points indicating values for each animal. $N = 2$ for same genotype pairs and $n = 5$ for multi-genotype pairs. Statistical analyses were performed using a two-way ANOVA with Tukey's or Sidak's post-hoc tests. For **d**, **e** unpaired *t*-test were completed $^{*}p < 0.05$; $^{**}p < 0.01$; $^{***}p < 0.001$. HD Huntington's disease; WT wild-type.

$HD^{(HD)}$ for both measures of diameter (Fig. S3d, e), indicating that sharing blood with an HD mouse detrimentally impacted the cortical vasculature despite the absence of changes in Collagen IV signal intensity. $HD^{(WT)}$ mice were similar to $HD^{(HD)}$ mice for all measures, except branch length (Fig. S3g). Here, partnership with a WT mouse substantially reduced the length of individual branches such that $HD^{(WT)}$ mice had similar branch length as WT controls. For vessel branching (Fig. S3f), while no significant differences were observed, a strong trend towards a reduction

was detected in $HD^{(WT)}$ mice. This reduction was well below all other groups which would generally indicate a detrimental change, except that it was coincident with the restoration of branch length which suggests the two findings may be linked. When treatment effects were assessed in the striatum, similar results for branch length were observed (Fig. 4g), but in this region, this did not reflect a return to $WT^{(WT)}$ values. In the striatum, both $WT^{(HD)}$ and $HD^{(WT)}$ groups were significantly lower than their respective control pairs suggesting that this effect was specific to animals partnered to a mouse of a different genotype. Finally, $HD^{(WT)}$ mice had improvements in blood vessel diameter, both in the absolute size and overall population (Fig. 4d, e). In both the striatum and the cortex, measures of diameter showed the clearest impact of partner blood. In the cortex, $WT^{(HD)}$ displayed significant impairments while in the striatum, $HD^{(WT)}$ mice demonstrated significant improvements. In both structures, the effects on branch length and number were more complex.

In addition to structural changes in blood vessels, increased permeability of the BBB has previously been described in mouse models of HD, including decreased expression of tight junction proteins, leakage and infiltration of leukocytes [45, 46]. Given the possible interactions between increased permeability and migration of peripheral cells into the brain, the effects of parabiosis on both of these factors was assessed using claudin 5, as an indicator of BBB permeability, and intercellular adhesion molecule (ICAM), as a marker of endothelial cell activation and recruitment of peripheral blood cells to the CNS. In the cortex, a significant effect of genotype was observed for claudin 5 (Fig. 5a) (Genotype: $F_{1,17} = 12.25$, $p = 0.0027$) but this phenomenon was not observed for ICAM (Genotype: $F_{1,17} = 0.7917$, $p = 0.3860$) (Fig. 5b), although $HD^{(WT)}$ mice had a significant increase in ICAM levels (Fig. 5b). These results are similar to those of the periphery suggesting that perfusion with healthy blood may yield protection against disease-associated pathology irrespective of site. In the striatum, no effect of genotype was observed for claudin 5 but parabiosis generated complex effects (Fig. 5c). $WT^{(WT)}$ mice had increased expression of claudin 5 compared with both $WT^{(NP)}$ and $WT^{(HD)}$. The difference between $WT^{(NP)}$ and $WT^{(WT)}$ is most likely the result of the parabiosis procedure. Since the $WT^{(HD)}$ and $WT^{(WT)}$ groups both underwent the same procedure, the decreased levels of claudin 5 in the $WT^{(HD)}$ mice could be a sign of increased vascular deficits in this model, as has been previously reported for R6/2 mice [45]. Similarly to claudin 5, ICAM levels were increased by the presence of parabiosis in $WT^{(WT)}$ mice but not in $WT^{(HD)}$ mice (Fig. 5d). The changes in markers of BBB integrity were associated with increased leakage, as measured by the presence of IgG antibodies in the parenchyma, in $HD^{(HD)}$ mice as compared with $WT^{(WT)}$ groups in both the cortex (Fig. 5e, f) and striatum (Fig. 5g, h). This increase was absent or reduced in $HD^{(WT)}$ in both structures, indicating a beneficial effect of sharing circulation with a WT mouse (Fig. 5e, g) (Interaction: Cortex $F_{2,20} = 198.8$, $p < 0.0001$; Striatum $F_{2,20} = 11.09$, $p = 0.0006$). The presence of this increase only in parabionts implies that the parabiosis procedure interacts with the genotype to specifically exacerbate barrier opening in the HD animals. The absence of this phenotype in $HD^{(WT)}$ mice indicates that this exacerbation is prevented by the presence of healthy blood.

In the context of HD, pathology in the CNS is the hallmark of disease phenotype and it is therefore critical to determine if the sharing of blood containing pathological elements also impacts this organ. To this end, western blots were performed in the cortex (Fig. 6a), striatum (Fig. S4a) and hippocampus (Fig. S4b) to determine if soluble mHTT was present, but no signal was detected in $WT^{(HD)}$ mice. However, an effect of parabiosis on the expression of WT HTT was seen as early as 6 months post-surgery in the cortex (Fig. 6a). At this time point, parabiosis decreased the expression of WT HTT in both HD and WT mice, with the greatest decreases present in $WT^{(HD)}$ and $HD^{(WT)}$ groups. Twelve months post-parabiosis, this pattern shifted and $WT^{(WT)}$ and $HD^{(HD)}$ had increased expression of WT HTT as compared with their respective non-parabiotic controls in the cortex (Fig. 6b). Support for the relevance of this decrease in soluble mHTT detected by western blot analysis comes from the FRASE assay which measures particularly toxic forms of the mHTT proteins [24]. Using this method, inclusion of $WT^{(NP)}$ material did not influence the aggregation of sensor proteins beyond what was observed in the buffer control (Fig. 6c, upper panel). However, the addition of lysates from both $HD^{(NP)}$ and $HD^{(WT)}$ groups accelerated the aggregation of sensor proteins indicating HTT seeds were present to accelerate the reaction kinetics (concentration-dependent left shift of the HD curves). Quantification of the seeding effects (Fig. 6c, lower panel) revealed a decrease in the seeding capacity in the $HD^{(WT)}$ group, suggesting a beneficial effect of the WT mouse on its partner in relation to cortical mHTT toxicity.

In the striatum, the only significant change was in WT HTT for $WT^{(HD)}$ mice where these animals had a significant increase as compared with the two control WT groups (Fig. S4a). In the hippocampus at 12 months, a similar decrease to that observed in the cortex at 6 months was detected in parabiotic animals, except $WT^{(WT)}$ mice, which displayed a decrease in WT HTT when compared with their non-parabiosis partner mice (Fig. S4b). Together, these findings suggest a complex interaction between parabiosis, genotype and partner genotype but all indicate that the parabiosis procedure itself impacts WT HTT in the brain. Western blots further showed a diminishment of mHTT in

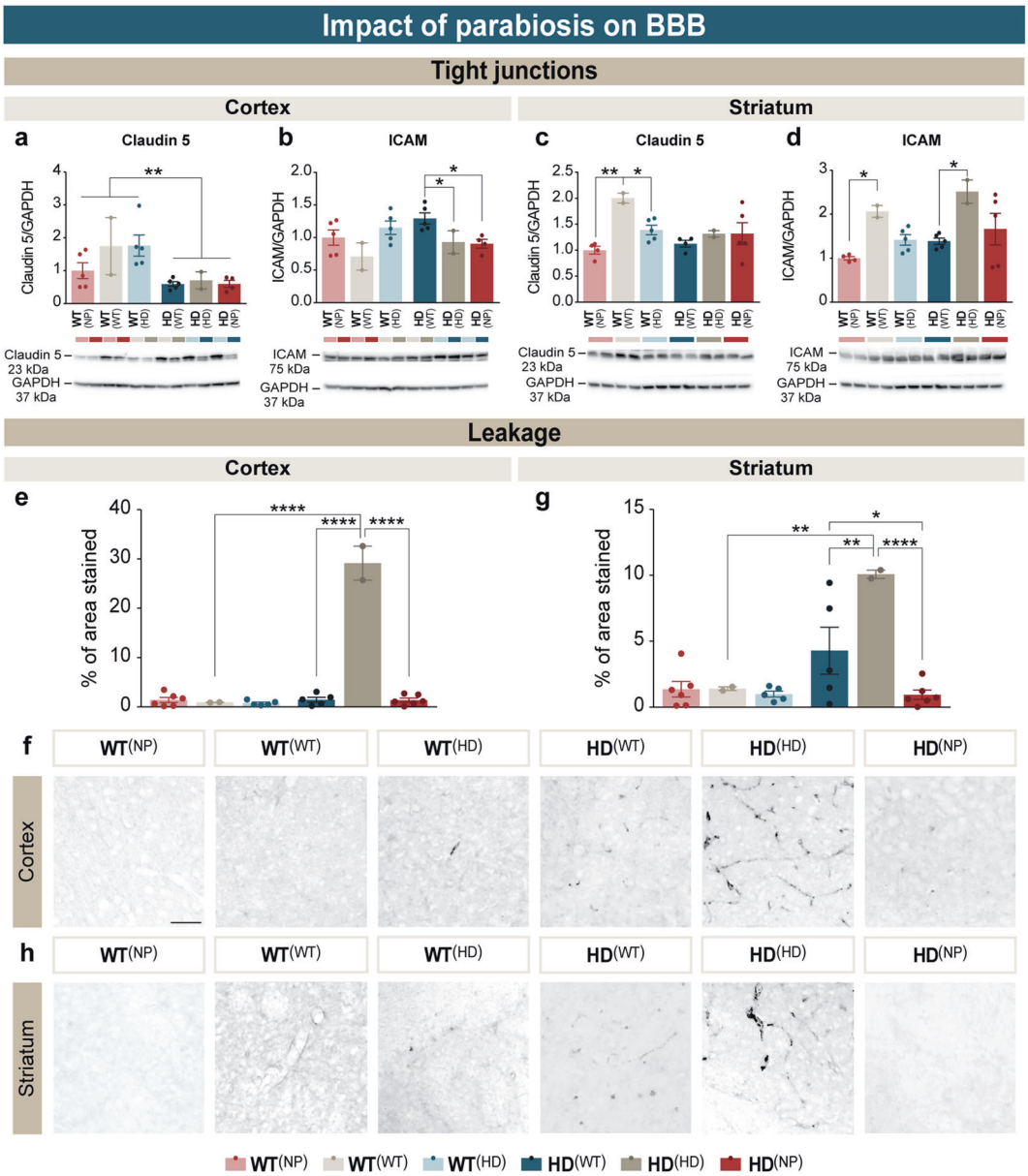

Fig. 5 BBB disruption in parabionts. Quantifications and immunoblots of tight junction proteins **a**, **c** claudin 5 and **b**, **d** ICAM measured in the **a**, **b** cortex and **c**, **d** striatum at 12 months post-surgery. **e, g** Quantifications and **f**, **h** representative images of immunohistochemical detection of IgG in the **e**, **f** cortex and **g**, **h** striatum of parabiotic mice 12 months post-surgery. Scale bar = 50 µm. Data are expressed as mean ± SEM with data points indicating values for each animal. $N = 2$ for same genotype pairs and $n = 5$ for multi-genotype pairs. Statistical analyses were performed using a two-way ANOVA with Tukey's post-hoc tests for all graphs except **b** for which a one-way ANOVA with Holm–Sidak's post-hoc test was used to analyze the HD groups. $^{*}p < 0.05$; $^{**}p < 0.01$; $^{****}p < 0.0001$. BBB blood–brain barrier, GAPDH Glyceraldehyde 3-phosphate dehydrogenase, HD Huntington's disease, ICAM intercellular adhesion molecule, IgG immunoglobulin G, kDa kilodalton, NP non-parabiotic mice, WT wild-type.

the cortex of HD$^{(WT)}$ mice but failed to detect an increase in mHTT in the same brain structure at 6 months post-surgery (Fig. 6a) or in the cortex, striatum and hippocampus 12 months post-surgery in WT$^{(HD)}$ mice (Figs. 6b and S4a, b). RT-qPCR analysis suggests that, similarly to the periphery, these changes occur at a post-transcriptional level, as no changes in mRNA were detected between any groups (Fig. S4d). Despite the absence of mHTT RNA and protein in WT$^{(HD)}$ mice, detection of insoluble mHTT by immunohistochemistry and filter retardation assay both indicate that mHTT is present in the brains of WT$^{(HD)}$ mice (Figs. 6d, e and S4c).

The presence of insoluble mHTT in the brain is strong evidence that mHTT can be transported from the circulatory system to the CNS but it does not indicate if there are functional consequences to this. To assess the potential impacts of

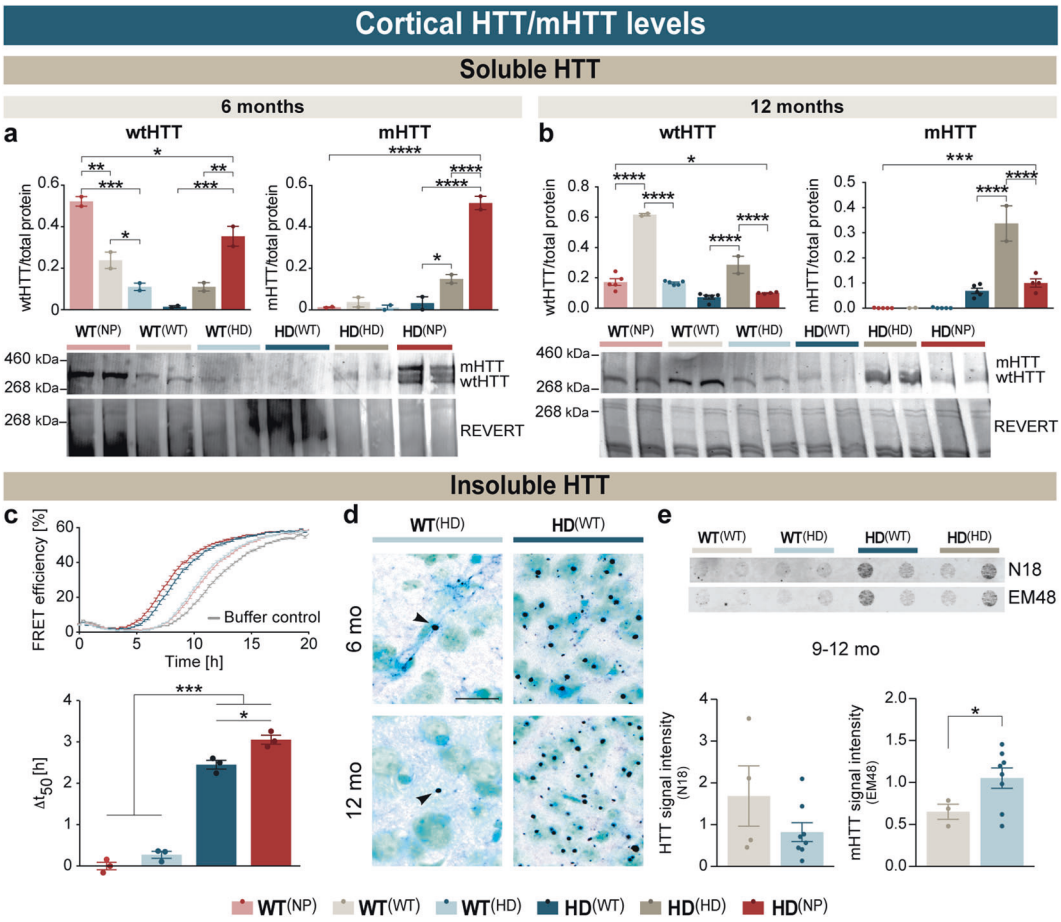

Fig. 6 Impact of parabiosis on cortical HTT/mHTT levels of parabionts. Quantifications and immunoblots of soluble HTT content at **a** 6 and **b** 12 months after parabiosis. **c** Quantification of the seeding capacity of the mHTT using a FRASE assay. **d** Representative images of immunohistochemical detection of EM48^{+} mHTT aggregates within the CNS (indicated by arrowheads). **e** Representative images (showing two animals per group) and quantifications of filter retardation assays of cortical samples 9 and 12 months post-surgery. Scale bar = 50 µm. Data are expressed as mean ± SEM with data points indicating values for each animal. $N = 2$ for same genotype pairs and $n = 5$ for multi-genotype pairs. Statistical analyses were performed using **a**, **b** a two-way ANOVA with Tukey's or Sidak's post-hoc tests or **e** unpaired students *t*-tests. For **c**, statistical significance was assessed by a one-way ANOVA followed by a Tukey's multiple comparison. $^{*}p < 0.05$; $^{**}p < 0.01$; $^{***}p < 0.001$; $^{****}p < 0.0001$. CNS central nervous system, EM48 anti-mHTT protein antibody, FRET fluorescence resonance energy transfer, h hour, HD Huntington's disease, HTT huntingtin protein, kDa kilodalton, m mutant, NP non-parabiotic mice, N18 anti-huntingtin protein antibody, WT wild-type.

mHTT in the cerebral tissue of parabionts, markers of various cell populations were assessed. In the cortex, NeuN [47], VGLUT1 [48, 49] and GAD65-67 [50, 51] were measured by western blot, as typical markers of cell populations targeted in HD. Consistent with disease features, an overall decrease was detected in NeuN (Fig. 7a) (Genotype: $F_{1,14} = 13.86$, $p = 0.0023$) and GAD65-67 in HD mice (Fig. 7c) (Genotype: $F_{1,13} = 20.15$, $p = 0.0006$), but not in VGLUT1 (Fig. 7b) (Genotype: $F_{1,15} = 0.3294$, $p = 0.5745$). For NeuN, no effect of parabiotic partner was observed in WT mice, but for GAD65-67, a decrease was detected in WT$^{(HD)}$ mice indicating that the presence of mHTT led to a detectable detrimental effect on this cellular population. Conversely, an improvement in HD$^{(WT)}$ mice was detected for both of these markers (Fig. 7a, c) but not for VGLUT1 (Fig. 7b). A similar analysis was performed in the striatum for corticostriatal terminals (VGLUT1) [49], projection neurons (DARPP32) [52] and interneurons (calretinin) [53]. A genotype specific decrease was absent in VGLUT1 (Genotype: $F_{1,13} = 3.808$, $p = 0.0729$) (Fig. 7d), DARPP32 (Fig. 7e) (Genotype: $F_{1,13} = 1.344$, $p = 0.2671$) and calretinin (Fig. 7f) (Genotype: $F_{1,14} = 1.247$, $p = 0.2828$). No change was detected in WT$^{(HD)}$ mice for any marker, but a protective effect in HD$^{(WT)}$ mice was observed for DARPP32, a well-established hallmark of pathology [54]. For this marker, an increase of signal intensity was present in HD$^{(WT)}$ as compared with both HD$^{(HD)}$ and HD$^{(NP)}$. The differences between VGLUT1 findings in the striatum and cortex suggests that the overall genotype effect observed in the cortex is not specifically linked to a change in the corticostriatal pathway, but may

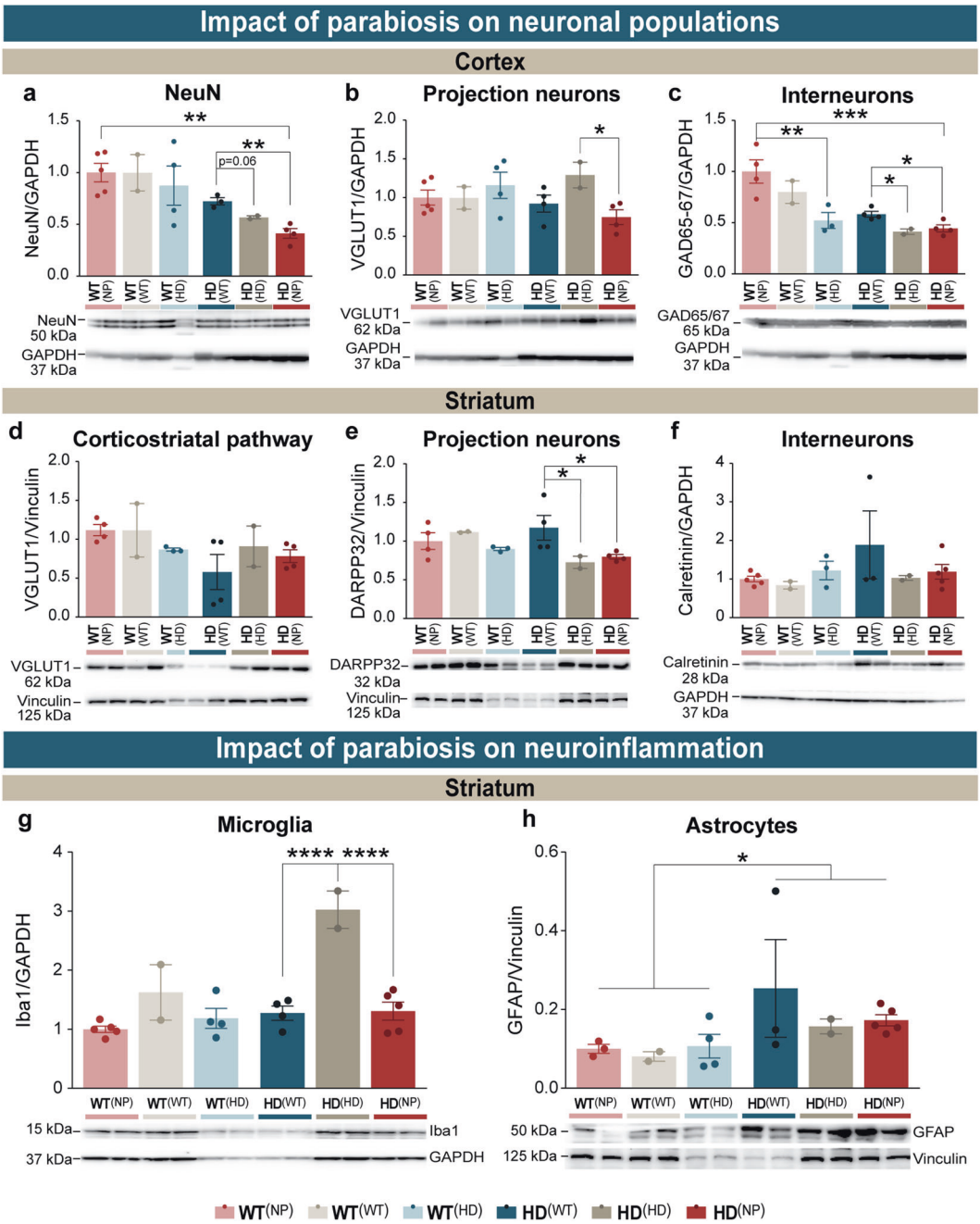

Fig. 7 Impact of parabiosis on neuronal and glial cell populations in parabionts. Quantifications and representative immunoblots of **a–c** cortical and **d–f** striatal neuronal markers as well as **g** microglia and **h** astrocytes assessed at 9 months post-surgery. Data are expressed as mean ± SEM with data points indicating values for each animal. N=2 for same genotype pairs and n=5 for multi-genotype pairs. Statistical analyses were performed using a two-way ANOVA with Tukey's or Sidak's post-hoc tests for all graphs except (**a**) for which a one-way ANOVA with Holm-Sidak's post-hoc test was used to analyze the HD groups. $*p<0.05$; $**p<0.01$; $***p<0.001$, $****p<0.0001$. DARPP32 Dopamine- and cAMP-regulated phosphoprotein 32, GAD65/67 Glutamic acid decarboxylase 65/67, GAPDH Glyceraldehyde 3-phosphate dehydrogenase, GFAP Glial fibrillary acidic protein, HD Huntington's disease, Iba1 Ionized calcium binding adapter molecule, kDa kilodalton, NeuN neuronal nuclei, NP non-parabiotic mice, VGLUT1 vesicular glutamate transporter 1, WT wild-type.

instead reflect changes in multiple pathways, such as corticocortical, corticothalamic and corticostriatal projections.

To better understand if the changes in cell markers by western blot reflected cell dysfunction or death, stereology was performed to count the number of calbindin$^+$ interneurons in the cortex as well as DARPP32$^+$ cells in the striatum (Fig. S5a, b). Calbindin was used for stereology as GAD65-67 staining is not conducive to counting and nearly

all calbindin^{+} cells in the neocortex are GABAergic interneurons, making these results comparable [55]. Both GAD65-67 protein expression and the number of calbindin^{+} neurons significantly differed between genotypes in the cortex (Genotype: $F_{1,15} = 6.086$, $p = 0.0262$) (Fig. S5a). In addition, HD$^{(WT)}$ mice still showed a strong trend towards an increase in cell number as compared with HD$^{(NP)}$. The largest difference between the two findings was the lack of significance between WT and HD groups by post-test in the cell count. For DARPP32, no group or treatment differences were detected in cell number (Genotype: $F_{1,14} = 0.2363$, $p = 0.6344$; Treatment: $F_{2,14} = 2.802$, $p = 0.0947$) (Fig. S5b). Overall, none of these cell counts showed a significant main effect of treatment, genotype or interaction. This was anticipated as changes in protein expression frequently occur prior to overt cell death and generally indicate changes in cell functionality.

Finally, the effect on non-neuronal cell types was measured by western blot detection of Iba1 and GFAP. For Iba1, a paradoxical increase was observed in WT$^{(WT)}$ mice compared with WT$^{(NP)}$ and WT$^{(HD)}$ mice (Fig. S6a). When microglia number was assessed in the same region, WT$^{(WT)}$ mice still differed, but in this case, a decrease was observed, although this did not reach statistical significance. When considered together, the two analyses are indicative of fewer cells with a higher concentration of Iba1 (Fig. S5c). No other genotype or group differences were observed for either marker in the cortex (Figs. S6a, b and S5c). In the striatum, HD$^{(HD)}$ mice demonstrated a significant increase in Iba1 which was absent in both HD$^{(WT)}$ and HD$^{(NP)}$ mice (Fig. 7g). No significant group differences were detected in the cell count (Fig. S5d). These findings suggest that parabiosis itself can increase microglial inflammation but this can be alleviated by the presence of blood from an animal of a different genotype. Only a minor genotype difference was measured for GFAP, although an increase was present in HD$^{(WT)}$ mice as compared with all other groups (Genotype: $F_{1,13} = 4.911$, $p = 0.0451$) (Fig. 7h).

In summary, the data indicate that the sharing of blood circulation between WT and HD mice has a number of consequences on both genotypes. In WT mice, propagation of mHTT was confirmed in both peripheral organs and the brain, and this propagation was associated with increased cellular and organ impairments including reduction of GAD65-67 expression and features of angiopathy (Fig. 8). In HD mice, these changes were largely beneficial and indicative of attenuated pathology. These improvements included decreased peripheral insoluble mHTT, decreased BBB leakage and increased expression of mitochondrial and neuronal disease-relevant markers (Fig. 8). To investigate potential mechanisms by which the improvements in HD$^{(WT)}$ mice and impairments in WT$^{(HD)}$ mice may be mediated, we tested two different hypotheses: (1) that changes in arterial blood pressure would promote an efflux of the mutant protein from the CSF to the blood and thus help its clearance and (2) that changes in peripheral inflammation may mediate both the central and peripheral effects. However, when we analyzed the different features of blood pressure in WT and transgenic animals (Fig. S7a–c), we did not observe significant differences except for heart rate (Fig. S7d). For inflammation, we focused our analysis on cytokines that have previously been reported to increase with disease progression such as interleukin-4 (IL-4), IL-5, IL-6, IL-10 and Tumor Necrosis Factor α (TNF-α) as well as cytokines which correlate with specific aspects of disease pathology such as TNF-α concentrations and the rate of motor symptom progression [19]. When we evaluated the plasma, all tested cytokines (excepting TNF-α) showed a trend towards an increase in WT$^{(HD)}$ mice, but only IL-4 and IL-10 reached statistical significance (Fig. S8a). This overall tendency suggests that an HD partner elevates disease-related cytokines in WT mice beyond what is expected from the surgical procedure. Since no differences were detected between WT$^{(NP)}$ and HD$^{(NP)}$ mice, this increase is unlikely to be an artifact due to high expression in the HD partner. This is further supported by the lack of change in HD$^{(WT)}$ animals although the parabiosis procedure itself showed a trend towards increased cytokines in both HD parabiotic groups (Fig. S8a). To determine if inflammation changes were present in organs, we also measured cytokines in the liver and kidney (Fig. S8b, c). In the liver, cytokines showed a robust genotype difference in the absence of significant effects of treatment (Fig. S8b). In the kidney (Fig. S8c), the effect of genotype was absent but an effect of treatment was present in IL-5 (Treatment: $F_{2,11} = 4.519$, $p=0.0369$) and TNF-α (Treatment: $F_{2,11} = 4.213$, $p=0.0438$), and approached significance for IL-4, 6 and 10 (Treatment: $F_{2,11} = 3.167$, $p=0.0820$, $F_{2,11} = 3.257$, $p=0.0775$, $F_{2,10} = 3.791$, $p=0.0595$ respectively). Together, these findings indicate that parabiosis impacts inflammation and that this modulation influences some, but not all, of the observed phenotypes.

Discussion

The work presented here was initiated to determine if the genetic product of HD, namely mHTT, could spread through the circulatory system and thereby cause disease-relevant pathological features. Using a parabiosis approach in which a surgical intervention allows two animals to share their circulatory systems, we demonstrate that mHTT protein and mRNA originating from an HD mouse can travel from the bloodstream into various tissues of a non-transgenic mouse; a phenomenon which extends to the appearance of signs of angiopathy and changes in neuronal markers in the brain of the WT animals. In addition to shedding light on the role of circulating mHTT in disease

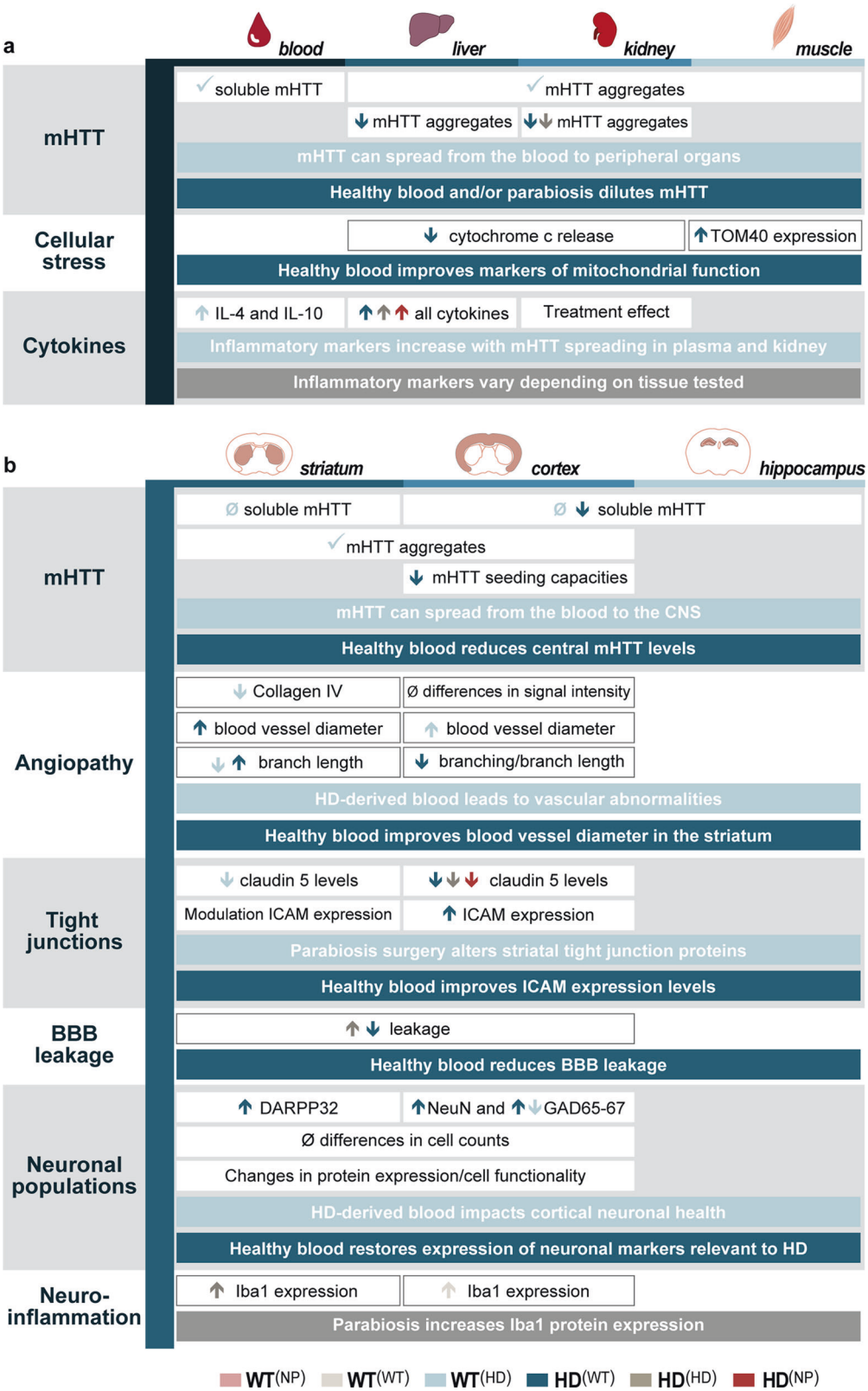

Fig. 8 Summary of findings. BBB blood–brain barrier, CNS central nervous system, DARPP32 dopamine- and cAMP-regulated phosphoprotein 32, GAD65/67 glutamic acid decarboxylase 65/67, HD huntington's disease, HTT huntingtin protein, Iba1 ionized calcium binding adapter molecule, ICAM intercellular adhesion molecule, IL interleukin, m mutant, NeuN neuronal nuclei, NP non-parabiotic mice, TOM40 translocase of the outer membrane 40, WT wild-type, √ presence, ∅ absence, ↑ increase, ↓ decrease.

dissemination, one of the critical findings of our experiment is the demonstration that sustained perfusion of healthy blood leads to improvements of several hallmarks of HD, both at the level of the periphery and brain.

In peripheral organs, insoluble mHTT aggregates were detectable within cells of all tested tissues as early as 6 months post-surgery. The presence of these aggregates confirms that mHTT can be taken up and retained by cells. However, this data does not discriminate whether the uptake is of whole aggregates, or if soluble mHTT is taken up and subsequently converted into an aggregate.

The most likely hypothesis is that free mHTT present in the plasma is transferred into the organs and over time, accumulates into aggregates. This process requires 6 months which is the same amount of time it takes for HTTExon1Q48 fibrils to induce behavioral changes after injection into the WT mouse brain [23]. This similarity in time suggests that seeding of soluble mHTT may indeed occur in both circumstances. While uptake of free mHTT has not previously been tested in vivo, a number of in vitro experiments have shown that free mHTT or HTT fibrils and protein fragments are taken up by a wide range of cells, including iPSC-derived neurons [23]. Furthermore, soluble mHTT, particularly fibrillar forms, is prone to spreading and therefore the most likely to result in pathological changes [56, 57]. While free plasma is a source of mHTT, soluble protein was also detected in all tested immune cells. These cells could have released mHTT into the organs via multiple pathways including through exocytosis [28] or the release of extracellular vesicles [58]. Previous evidence has demonstrated that both exocytosis and extracellular vesicles can contribute to mHTT spreading in HD. A role of exocytosis was observed in a Drosophila model of HD where spreading of aggregates and neuronal loss was prevented by selective genetic crosses which lead to the elimination of essential exocytosis proteins [28], while injection of extracellular vesicles derived from HD patient fibroblasts to the brains of WT mice was shown to induce severe motor impairments and detection of EM48 positive signal in the brains of WT mice [9]. Of these two possibilities, extracellular vesicles would best explain the presence of mHTT within the striatum and cortex of $WT^{(HD)}$ mice as peripherally produced vesicles have been demonstrated to cross the BBB and to enter the CNS [59]. One point of evidence against this is the lack of detectable soluble mHTT within peripheral organs. However, it is possible the soluble mHTT is present but at levels below the sensitivity threshold of western blot. The possibility that mHTT aggregates are directly transferred from immune cells is less likely, as very few reports have described the presence of vesicles in peripheral immune cells [32] and directly deposited aggregates would likely be degraded before causing lasting harm to the cellular elements.

The findings discussed above raise important questions regarding the possibility of transmission of mHTT in clinical settings. Currently, patients with neurodegenerative disorders are not excluded from blood or organ donation but given the accumulating evidence that many pathological proteins associated with neurodegenerative diseases are capable of spreading and causing pathological changes [60, 61], it is important to understand if there is a risk associated with these procedures. In the context of HD, the required 6-month period of continuous blood infusion used in this study makes any clinical risk of transmitting disease by blood transfusion very low. These findings are in line with previous reports examining the risk of developing Alzheimer's disease in individuals that have received blood transfusion from patients diagnosed with this disease [62]. While transmission of HD by blood transfusion is improbable, the risk after organ transplantation is less clear. It is possible that transplantation of an organ from an HD patient could have detrimental effects, as liver transplants from familial amyloid polyneuropathy and amyotrophic lateral sclerosis has been shown to result in the presence of disease-associated proteins in the graft recipients [63, 64]. Based on our results, full-blown disease would still be extremely unlikely, as toxicity of mHTT in the parabiosis model was limited. Behavioral testing would be necessary to draw firm conclusions, but this is rendered impracticable as the animals of the same pair interact extensively together, adapting their behavior to their partner, thus making the discrimination of the results impossible [42].

Contrary to the detrimental effects observed in WT mice, our data strongly suggests that healthy blood may have a therapeutic effect on HD mice. In the liver, $HD^{(WT)}$ mice had half the number of aggregates as either $HD^{(HD)}$ or $HD^{(NP)}$. In the muscle, WT blood did not impact the number of aggregates but it did significantly improve the mitochondrial function. A particularly interesting part of this data was the dose-response pattern where $HD^{(NP)}$ displayed the greatest difference from WT with slight improvements detected in $HD^{(HD)}$ and the strongest in $HD^{(WT)}$. Such a pattern of change was not only present in the periphery but was also detected in HTT levels in the brain at 6 months where the concentration of WT HTT and mHTT decreased substantially from NP mice to same genotype pairs, and from same genotype pairs to two genotype pairs. The presence of such striking changes in both the periphery and CNS strongly suggests that the parabiosis procedure may modulate HTT itself. Over time, this effect stabilized and by 12 months post-parabiosis, same genotype couples had a marked increase in both mHTT and WT HTT. Given the absence of changes in mRNA levels in the brain, it seems likely that the mechanism involved in mHTT reduction involves increased protein degradation. This dose-response pattern was also observed in NeuN levels in the cortex but other protein changes, such as GAD65/67

and DARPP32, were only observed in $HD^{(WT)}$ mice. When the combination of cell counts and differences in protein levels are examined together, the results are indicative of functional changes to DARPP32 and Iba1 in the striatum and GAD65/67 in the cortex, which supports the beneficial effect of WT blood on HD mice. The changes observed in DARPP32 are particularly informative, especially when considered with western blot data of VGLUT1, as both of these proteins are associated with the corticostriatal pathway. The changes in DARPP32 protein are supportive of this, but VGLUT1 alterations in the cortex and striatum indicate that multiple pathways may be impacted. Parabiosis itself increases VGLUT1 in the cortex in a manner which is seemingly independent of WT blood, while no significant effect of parabiosis or WT blood is apparent in the striatum. This may suggest that there are two separate effects: one on projection neurons of the cortex and one on DARPP32 positive striatal projection neurons. Overall, the different changes observed between various proteins imply that multiple mechanisms are involved in these beneficial changes.

Biomarker studies have reported that the concentration of mHTT in the CSF correlates well with disease stage and severity [10], suggesting that a reduction of mHTT in the CSF would be likely to have clinical benefits. Whether peripheral concentrations of mHTT impact CSF levels is unclear, recent studies reducing mHTT to 50% in peripheral organs in a mouse model of HD did not result in any improvements to central pathology [65]. However, it should be noted that this particular study did not evaluate whether HTT/mHTT was reduced within cells of the immune system and used the Q111 mouse model which presents with a rather mild phenotype [66]. A second possibility is that the parabiosis procedure itself contributes to clearance of toxic substances from the CNS by lowering blood pressure and thereby favoring efflux of CSF. This would be consistent with the "dose response" effect observed for some CNS changes (i.e., HTT and NeuN). Evidence from the literature is limited but one study of rats in parabiosis measured blood pressure and failed to detect a decrease. However, this study was completed with hypertensive and normotensive rats which decreases the ability to extrapolate to a situation where both animals are normotensive at the start of the study [67]. The lack of striking differences between zQ175 and WT animals suggests that this mechanism is unlikely to be important in the benefits observed, although it is conceivable that combining the two genotypes could result in hemodynamic alterations that are not present under basal conditions. A third possibility would be that blood from the WT mouse is diluting inflammatory cytokines or other detrimental circulating factors, thereby modifying disease phenotypes. This hypothesis is supported by several studies which have described a relationship between peripheral plasma levels of cytokines and disease progression or HTT levels [19]. Additionally, multiple cytokines have been shown to increase with disease progression including IL-4, IL-5, and IL-10 [19]. When we measured cytokines in the plasma, we did not see a significant reduction in $HD^{(WT)}$ mice although $WT^{(HD)}$ animals had consistently showed a trend towards an increase in circulating cytokines, suggesting that inflammation may contribute to the detrimental changes observed.

While further work is required to clarify the mechanism underlying the beneficial effects of healthy blood on disease-related features, our findings suggest that some form of blood transfusion or plasma exchange may result in meaningful clinical benefits in patients. Due to the amount of time required for improvements in our model, transfusions alone would not be sufficient but plasmapheresis, a process similar to dialysis designed to replace plasma from patients with healthy plasma, may be of use by either reducing mHTT or normalizing plasma levels of cytokines [20, 68, 69]. This method has already been studied for brain rejuvenation, namely with heterochronic parabiosis between an elderly mouse and a young mouse [70, 71] and clinical studies are devoted to this new Fountain of Youth, whose initial results have demonstrated the safety, tolerability and feasibility of this intervention [72]. Given the large number of factors impacted by parabiosis, assessment of the clinical effects of plasmapheresis in HD would be warranted and may have implications for other disorders of the CNS.

Taken together, the results of our parabiosis study provide clear evidence that blood can serve as a vehicle for mHTT propagation, which leads to mild HD-related pathology. The most obvious explanation for this propagation is the presence of mHTT in free forms in the plasma which can then be taken up by cells. Our findings are also of significant clinical importance in that we have shown that healthy blood can abrogate a number of pathological features of HD mice. This suggests that targeting peripheral blood circulation may be a novel and effective therapeutic strategy for HD.

Acknowledgements FC is a recipient of a Researcher Chair from the Fonds de Recherche du Québec en Santé (FRQS) providing salary support and operating funds, and receives funding from the Canadian Institutes of Health Research (CIHR) to conduct her HD-related research. At this time of the study, MR and HLD were supported by a Desjardins scholarships from the Fondation du CHU de Québec, and later by doctoral training scholarships from the FRQS. GS is supported by a doctoral training scholarship from the FRQS and MA by a post-doctoral fellowship from the same funding agency. Sincere thanks to Dr. Gillian Bates for generously providing the S829 antibody.

Compliance with ethical standards

Conflict of interest The authors declare that they have no conflict of interest.

References

1. Phillips W, Shannon KM, Barker RA. The current clinical management of Huntington's disease. Mov Disord. 2008;23:1491–504.
2. Papp KV, Kaplan RF, Snyder PJ. Biological markers of cognition in prodromal Huntington's disease: a review. Brain Cogn. 2011;77:280–91.
3. Tang C, Feigin A. Monitoring Huntington's disease progression through preclinical and early stages. Neurodegener Dis Manag. 2012;2:421–35.
4. Reiner A, Dragatsis I, Dietrich P. Genetics and neuropathology of Huntington's disease. Int Rev Neurobiol. 2011;98:325–72.
5. Vonsattel JPG, Keller C, Del Pilar, Amaya M. Neuropathology of Huntington's disease. Handb Clin Neurol. 2008;89:599–618.
6. Venkatraman P, Wetzel R, Tanaka M, Nukina N, Goldberg AL. Eukaryotic proteasomes cannot digest polyglutamine sequences and release them during degradation of polyglutamine-containing proteins. Mol Cell. 2004;14:95–104.
7. Jana NR, Zemskov EA, Wang G, Nukina N. Altered proteasomal function due to the expression of polyglutamine-expanded truncated N-terminal huntingtin induces apoptosis by caspase activation through mitochondrial cytochrome c release. Hum Mol Genet. 2001;10:1049–59.
8. Davies SW, Turmaine M, Cozens BA, DiFiglia M, Sharp AH, Ross CA, et al. Formation of neuronal intranuclear inclusions underlies the neurological dysfunction in mice transgenic for the HD mutation. Cell. 1997;90:537–48.
9. Jeon I, Cicchetti F, Cisbani G, Lee S, Li E, Bae J, et al. Human-to-mouse prion-like propagation of mutant huntingtin protein. Acta Neuropathol 2016;132:577–92.
10. Wild EJ, Boggio R, Langbehn D, Robertson N, Haider S, Miller JR, et al. Quantification of mutant huntingtin protein in cerebrospinal fluid from Huntington's disease patients. J Clin Investig. 2015;125:1979–86.
11. Cicchetti F, Lacroix S, Cisbani G, Vallieres N, Saint-Pierre M, St-Amour I, et al. Mutant huntingtin is present in neuronal grafts in Huntington disease patients. Ann Neurol. 2014;76:31–42.
12. Liu X, Valentine SJ, Plasencia MD, Trimpin S, Naylor S, Clemmer DE. Mapping the human plasma proteome by SCX-LC-IMS-MS. J Am Soc Mass Spectrom. 2007;18:1249–64.
13. Gutekunst CA, Li SH, Yi H, Mulroy JS, Kuemmerle S, Jones R, et al. Nuclear and neuropil aggregates in Huntington's disease: relationship to neuropathology. J Neurosci. 1999;19:2522–34.
14. Vonsattel JP, Myers RH, Stevens TJ, Ferrante RJ, Bird ED, Richardson EP Jr. Neuropathological classification of Huntington's disease. J Neuropathol Exp Neurol. 1985;44:559–77.
15. Saudou F, Humbert S. The biology of huntingtin. Neuron. 2016;89:910–26.
16. Stuwe SH, Goetze O, Lukas C, Klotz P, Hoffmann R, Banasch M, et al. Hepatic mitochondrial dysfunction in manifest and premanifest Huntington disease. Neurology. 2013;80:743–6.
17. Caviston JP, Holzbaur ELF. Huntingtin as an essential integrator of intracellular vesicular trafficking. Trends Cell Biol. 2009;19:147–55.
18. Weiss A, Trager U, Wild EJ, Grueninger S, Farmer R, Landles C, et al. Mutant huntingtin fragmentation in immune cells tracks Huntington's disease progression. J Clin Investig. 2012;122:3731–6.
19. Bjorkqvist M, Wild EJ, Thiele J, Silvestroni A, Andre R, Lahiri N, et al. A novel pathogenic pathway of immune activation detectable before clinical onset in Huntington's disease. J Exp Med. 2008;205:1869–77.
20. Kwan W, Magnusson A, Chou A, Adame A, Carson MJ, Kohsaka S, et al. Bone marrow transplantation confers modest benefits in mouse models of Huntington's disease. J Neurosci. 2012;32:133–42.
21. Jimenez-Sanchez M, Licitra F, Underwood BR, Rubinsztein DC. Huntington's disease: mechanisms of pathogenesis and therapeutic strategies. Cold Spring Harb Perspect Med. 2017;7:a024240.
22. Masnata M, Cicchetti F. The evidence for the spread and seeding capacities of the mutant huntingtin protein in in vitro systems and their therapeutic implications. Front Neurosci. 2017;11:647.
23. Masnata M, Sciacca G, Maxan A, Bousset L, Denis HL, Lauruol F, et al. Demonstration of prion-like properties of mutant huntingtin fibrils in both in vitro and in vivo paradigms. Acta Neuropathol. 2019;137:981–1001.
24. Ast A, Buntru A, Schindler F, Hasenkopf R, Schulz A, Brusendorf L, et al. mHTT seeding activity: a marker of disease progression and neurotoxicity in models of Huntington's disease. Mol Cell. 2018;71:675–688.e6.
25. Wagner AS, Politi AZ, Ast A, Bravo-Rodriguez K, Baum K, Buntru A, et al. Self-assembly of mutant huntingtin exon-1 fragments into large complex fibrillar structures involves nucleated branching. J Mol Biol. 2018;430:1725–44.
26. Ko J, Isas JM, Sabbaugh A, Yoo JH, Pandey NK, Chongtham A, et al. Identification of distinct conformations associated with monomers and fibril assemblies of mutant huntingtin. Hum Mol Genet. 2018;27:2330–43.
27. Kim D-K, Cho K-W, Ahn WJ, Perez-Acuña D, Jeong H, Lee H-J, et al. Cell-to-cell transmission of polyglutamine aggregates in C. elegans. Exp Neurobiol. 2017;26:321–8.
28. Babcock DT, Ganetzky B. Transcellular spreading of huntingtin aggregates in the Drosophila brain. Proc Natl Acad Sci. 2015;112:E5427–33.
29. Menalled LB, Kudwa AE, Miller S, Fitzpatrick J, Watson-Johnson J, Keating N, et al. Comprehensive behavioral and molecular characterization of a new knock-in mouse model of Huntington's disease: zQ175. PLoS One. 2012;7:e49838.
30. Kamran P, Sereti KI, Zhao P, Ali SR, Weissman IL, Ardehali R. Parabiosis in mice: a detailed protocol. J Vis Exp. 2013;80:50556.
31. Garneau AP, Marcoux A-A, Noël M, Frenette-Cotton R, Drolet M-C, Couet J, et al. Ablation of potassium-chloride cotransporter type 3 (Kcc3) in mouse causes multiple cardiovascular defects and isosmotic polyuria. PloS One. 2016;11:e0154398.
32. Denis HL, Lamontagne-Proulx J, St-Amour I, Mason SL, Rowley JW, Cloutier N, et al. Platelet abnormalities in Huntington's disease. J Neurol Neurosurg Psychiatry. 2019;90:272–83.
33. Marcoux G, Duchez A-C, Cloutier N, Provost P, Nigrovic PA, Boilard E. Revealing the diversity of extracellular vesicles using high-dimensional flow cytometry analyses. Sci Rep. 2016;6:35928.
34. Tremblay C, Pilote M, Phivilay A, Emond V, Bennett DA, Calon F. Biochemical characterization of Abeta and tau pathologies in mild cognitive impairment and Alzheimer's disease. J Alzheimers Dis. 2007;12:377–90.

35. Tung JW, Heydari K, Tirouvanziam R, Sahaf B, Parks DR, Herzenberg LA, et al. Modern flow cytometry: a practical approach. Clin Lab Med. 2007;27:453–68.
36. Bustin SA, Benes V, Garson JA, Hellemans J, Huggett J, Kubista M, et al. The MIQE guidelines: minimum information for publication of quantitative real-time PCR experiments. Clin Chem. 2009;55:611–22.
37. Livak KJ, Schmittgen TD. Analysis of relative gene expression data using real-time quantitative PCR and the $2-\Delta\Delta CT$ method. Methods. 2001;25:402–8.
38. Arganda-Carreras I, Fernández-González R, Muñoz-Barrutia A, Ortiz-De-Solorzano C. 3D reconstruction of histological sections: application to mammary gland tissue. Microsc Res Technol. 2010;73:1019–29.
39. Miller JRC, Pfister EL, Liu W, Andre R, Träger U, Kennington LA, et al. Allele-selective suppression of mutant huntingtin in primary human blood cells. Sci Rep. 2017;7:46740.
40. Shirendeb U, Reddy AP, Manczak M, Calkins MJ, Mao P, Tagle DA, et al. Abnormal mitochondrial dynamics, mitochondrial loss and mutant huntingtin oligomers in Huntington's disease: implications for selective neuronal damage. Hum Mol Genet. 2011;20:1438–55.
41. Choo YS, Johnson GVW, MacDonald M, Detloff PJ, Lesort M. Mutant huntingtin directly increases susceptibility of mitochondria to the calcium-induced permeability transition and cytochrome c release. Hum Mol Genet. 2004;13:1407–20.
42. Bu XL, Xiang Y, Jin WS, Wang J, Shen LL, Huang ZL, et al. Blood-derived amyloid-beta protein induces Alzheimer's disease pathologies. Mol Psych. 2017;23:1948–56.
43. Merlini M, Wanner D, Nitsch RM. Tau pathology-dependent remodelling of cerebral arteries precedes Alzheimer's disease-related microvascular cerebral amyloid angiopathy. Acta Neuropathol. 2016;131:737–52.
44. Uspenskaia O, Liebetrau M, Herms J, Danek A, Hamann GF. Aging is associated with increased collagen type IV accumulation in the basal lamina of human cerebral microvessels. BMC Neurosci. 2004;5:37.
45. Drouin-Ouellet J, Sawiak SJ, Cisbani G, Lagace M, Kuan WL, Saint-Pierre M, et al. Cerebrovascular and blood-brain barrier impairments in Huntington's disease: potential implications for its pathophysiology. Ann Neurol. 2015;78:160–77.
46. Di Pardo A, Amico E, Scalabrì F, Pepe G, Castaldo S, Elifani F, et al. Impairment of blood-brain barrier is an early event in R6/2 mouse model of Huntington disease. Sci Rep. 2017;7:41316.
47. Slow EJ, van Raamsdonk J, Rogers D, Coleman SH, Graham RK, Deng Y, et al. Selective striatal neuronal loss in a YAC128 mouse model of Huntington disease. Hum Mol Genet. 2003;12:1555–67.
48. Deng YP, Wong T, Bricker-Anthony C, Deng B, Reiner A. Loss of corticostriatal and thalamostriatal synaptic terminals precedes striatal projection neuron pathology in heterozygous Q140 Huntington's disease mice. Neurobiol Dis. 2013;60:89–107.
49. Deng Y-P, Wong T, Wan JY, Reiner A. Differential loss of thalamostriatal and corticostriatal input to striatal projection neuron types prior to overt motor symptoms in the Q140 knock-in mouse model of Huntington's disease. Front Syst Neurosci. 2014;8:198.
50. Hsu Y-T, Chang Y-G, Chern Y. Insights into GABAAergic system alteration in Huntington's disease. Open Biol. 2018;8:180165.
51. Han I, You Y, Kordower JH, Brady ST, Morfini GA. Differential vulnerability of neurons in Huntington's disease: the role of cell type-specific features. J Neurochem. 2010;113:1073–91.
52. Cicchetti F, Gould PV, Parent A. Sparing of striatal neurons coexpressing calretinin and substance P (NK1) receptor in Huntington's disease. Brain Res. 1996;730:232–7.
53. Parent A, Cicchetti F, Beach TG. Calretinin-immunoreactive neurons in the human striatum. Brain Res. 1995;674:347–51.
54. van Dellen A, Welch J, Dixon RM, Cordery P, York D, Styles P, et al. N-Acetylaspartate and DARPP-32 levels decrease in the corpus striatum of Huntington's disease mice. Neuroreport. 2000;11:3751–7.
55. DeFelipe J. Types of neurons, synaptic connections and chemical characteristics of cells immunoreactive for calbindin-D28K, parvalbumin and calretinin in the neocortex. J Chem Neuroanat. 1997;14:1–19.
56. Kim YE, Hosp F, Frottin F, Ge H, Mann M, Hayer-Hartl M, et al. Soluble oligomers of polyQ-expanded huntingtin target a multiplicity of key cellular factors. Mol Cell. 2016;63:951–64.
57. Leitman J, Ulrich Hartl F, Lederkremer GZ. Soluble forms of polyQ-expanded huntingtin rather than large aggregates cause endoplasmic reticulum stress. Nat Commun. 2013;4:2753.
58. Tang BL. Unconventional secretion and intercellular transfer of mutant huntingtin. Cells. 2018;7:E59.
59. Rufino-Ramos D, Albuquerque PR, Carmona V, Perfeito R, Nobre RJ, Pereira, de Almeida L. Extracellular vesicles: novel promising delivery systems for therapy of brain diseases. J Controlled Release. 2017;262:247–58.
60. Jucker M, Walker LC. Self-propagation of pathogenic protein aggregates in neurodegenerative diseases. Nature. 2013;501:45–51.
61. Soto C. Transmissible proteins: expanding the prion heresy. Cell. 2012;149:968–77.
62. Edgren G, Hjalgrim H, Rostgaard K, Lambert P, Wikman A, Norda R, et al. Transmission of neurodegenerative disorders through blood transfusion: a cohort study. Ann Intern Med. 2016;165:316–24.
63. Llado L, Baliellas C, Casasnovas C, Ferrer I, Fabregat J, Ramos E, et al. Risk of transmission of systemic transthyretin amyloidosis after domino liver transplantation. Liver Transpl. 2010;16:1386–92.
64. Holmes BB, Diamond MI. Amyotrophic lateral sclerosis and organ donation: is there risk of disease transmission? Ann Neurol. 2012;72:832–6.
65. Coffey SR, Bragg RM, Minnig S, Ament SA, Cantle JP, Glickenhaus A, et al. Peripheral huntingtin silencing does not ameliorate central signs of disease in the B6.HttQ111/+ mouse model of Huntington's disease. PloS One 2017;12:e0175968.
66. Menalled L, El-Khodor BF, Patry M, Suárez-Fariñas M, Orenstein SJ, Zahasky B, et al. Systematic behavioral evaluation of Huntington's disease transgenic and knock-in mouse models. Neurobiol Dis. 2009;35:319–36.
67. Zidek W, Ottens E, Heckmann U. Transmission of hypertension in rats by cross circulation. Hypertension. 1989;14:61–5.
68. Bouwens JA, van Duijn E, Cobbaert CM, Roos RAC, van der Mast RC, Giltay EJ. Plasma cytokine levels in relation to neuropsychiatric symptoms and cognitive dysfunction in Huntington's disease. J Hunt Dis. 2016;5:369–77.
69. Rocha NP, Ribeiro FM, Furr-Stimming E, Teixeira AL. Neuroimmunology of Huntington's disease: revisiting evidence from human studies. Mediators Inflamm. 2016;2016:8653132.
70. Villeda SA, Plambeck KE, Middeldorp J, Castellano JM, Mosher KI, Luo J, et al. Young blood reverses age-related impairments in cognitive function and synaptic plasticity in mice. Nat Med. 2014;20:659–63.
71. Horowitz AM, Villeda SA. Therapeutic potential of systemic brain rejuvenation strategies for neurodegenerative disease. F1000 Res. 2017;6:1291.
72. Sha SJ, Deutsch GK, Tian L, Richardson K, Coburn M, Gaudioso JL, et al. Safety, tolerability, and feasibility of young plasma infusion in the plasma for Alzheimer symptom amelioration study: a randomized clinical trial. JAMA Neurol. 2019;76:35–40.